

Transmission operators for the non-overlapping Schwarz method for solving Helmholtz problems in rectangular cavities

Nicolas Marsic^{a,*}, Christophe Geuzaine^b, Herbert De Gerssem^a

^a*Technische Universität Darmstadt, Institute for Accelerator Science and Electromagnetic Fields (TEMF), D-64289 Darmstadt, Germany*

^b*Université de Liège, Institut Montefiore B28, B-4000 Liège, Belgium*

Abstract

In this paper we discuss different transmission operators for the non-overlapping Schwarz method which are suited for solving the time-harmonic Helmholtz equation in cavities (*i.e.* closed domains which do not feature an outgoing wave condition). Such problems are heavily impacted by back-propagating waves which are often neglected when devising optimized transmission operators for the Schwarz method. This work explores new operators taking into account those back-propagating waves and compares them with well-established operators neglecting these contributions. Notably, this paper focuses on the case of rectangular cavities, as the optimal (non-local) transmission operator can be easily determined. Nonetheless, deviations from this ideal geometry are considered as well. In particular, computations of the acoustic noise in a three-dimensional model of the helium vessel of a beamline cryostat with optimized Schwarz schemes are discussed. Those computations show a reduction of 46% in the iteration count, when comparing an operator optimized for cavities with those optimized for unbounded problems.

Keywords: domain decomposition method, optimized Schwarz method, Helmholtz equation, cavity problem

2000 MSC: 65N55, 65N22, 65F10

1. Introduction

It is well known that large-scale time-harmonic Helmholtz problems are hard to solve because of *i*) the pollution effect [1] and *ii*) the indefiniteness of the discretized operator [2]. While the pollution effect can be alleviated by using higher order discretization schemes [3], the indefiniteness is an intrinsic property of time-harmonic wave problems, at least with standard variational formulations [4, 5], and significantly limits the performance of classical iterative solvers, such as the generalized minimal residual method (GMRES) for instance. Of course, as an alternative to iterative algorithms, direct solvers can be used. However, because of the fill-in effect, whose minimization is known to be a NP-complete problem [6], the amount of memory needed to treat large-scale systems can become prohibitively high (see for instance [7]).

As an alternative to direct and (unpreconditioned) iterative methods for solving large-scale, high-frequency time-harmonic Helmholtz problems, domain decomposition (DD) algorithms, and optimized Schwarz (OS) techniques [8–11] in particular, have attracted a lot of attention during the last decades. The key idea thereof is: *i*) to decompose the computational domain into (possibly overlapping) subdomains, creating thus new subproblems, *ii*) to solve each subproblem *independently*, *iii*) to exchange data at the interfaces between the subdomains via an appropriate *transmission operator* and *iv*) to repeat this “solve and exchange” procedure until convergence of the solution. Since all subproblems are solved independently,

*Corresponding author

Email addresses: marsic@temf.tu-darmstadt.de (Nicolas Marsic), cgeuzaine@uliege.be (Christophe Geuzaine), degerssem@temf.tu-darmstadt.de (Herbert De Gerssem)

domain decomposition methods are parallel by nature¹ and are thus very well suited for the treatment of large-scale problems. Furthermore, as the subproblems are of reduced size, direct solvers can be used. Let also note that DD methods are rarely used as stand-alone solvers, but most of the time as a *preconditioner* for a Krylov subspace method such as GMRES. The design of such preconditioners for time-harmonic Helmholtz problems remains an active and challenging topic [13].

The convergence rate of an OS scheme strongly depends on its transmission operator. It is well known that the optimal operator is the Dirichlet-to-Neumann (DtN) map at the interface between two subdomains [14] (*i.e.* the operator relating the trace of the unknown field to its normal derivative at a given interface). However, the DtN map is rarely employed, as it is a *non-local* operator which leads to a numerically expensive scheme. Instead, in practice, *local approximations* of the DtN map are used, which lead to many different computational schemes [8–11]. To the best of our knowledge, those OS techniques share a common drawback: they ignore the impact of *back-propagating waves*. While this assumption is legitimate in many cases (antenna arrays [15], medical imaging reconstruction [16] or photonic waveguides [17] just to cite a few), it becomes questionable when the geometry allows resonances (even if the source does not oscillate exactly at a resonance frequency), as found for instance in lasers [18], accelerator cavities [19] or quantum electrodynamic devices [7].

The objective of this work is to develop new transmission conditions taking into account the effect of back-propagating waves, and to compare them with well-established operators neglecting these contributions. To this end, we will study a rectangular cavity, determine the DtN map and localize it by following different strategies. We will then apply the resulting new transmission operators to more general geometries. This paper is organized as follows. In sections 2 and 3 the model problem with Dirichlet boundary conditions and the associated DtN map are presented for both overlapping and non-overlapping decompositions. New transmission operators are afterwards presented in section 4 and generalized (*i.e.* multiple subdomains and Neumann boundary conditions) in section 5. This is followed by section 6 showing a comparison with the classical DtN map related to unbounded problems and the use of transmission operators optimized for unbounded problems as an approximation of the *cavity* DtN map. The new transmission operators are then validated and compared with numerical experiments involving the reference rectangular cavity in section 7. The case of geometries deviating from this last model problem is further discussed in section 8 and an engineering problem involving a model of the helium vessel of a beamline cryostat is analyzed in section 9. Finally, conclusions are drawn in section 10.

2. Model problem and Schwarz domain decomposition method

Let Ω be the two-dimensional domain $[-\ell/2, +\ell/2] \times [0, h]$ depicted in Figure 1a, and let $\Gamma = \Gamma_l \cup \Gamma_w \cup \Gamma_r$ be its boundary. This domain is separated into two non-overlapping subdomains $\Omega_0 = [-\ell/2, \gamma(t)] \times [0, h]$ and $\Omega_1 = [\gamma(t), +\ell/2] \times [0, h]$, where $\gamma(t) = t\ell - \ell/2$ with $t \in [0, 1]$ a fixed parameter controlling the position of the interface shared by the two subdomains, as shown in Figure 1b. In addition, the resulting subdomains have a length of ℓ_{01} (for Ω_0) and ℓ_{10} (for Ω_1) respectively and $\ell = \ell_{01} + \ell_{10}$. This splitting has introduced a new artificial boundary on each subdomain: we denote by Σ_{01} the artificial boundary of Ω_0 and by Σ_{10} the artificial boundary of Ω_1 . Furthermore, \mathbf{n}_{ij} denotes the outwardly oriented unit vector normal to Σ_{ij} .

Let us solve the following Helmholtz problem on Ω :

$$\begin{cases} \operatorname{div} \mathbf{grad} p + k^2 p = g & \text{on } \Omega, \\ p = 0 & \text{on } \Gamma, \end{cases} \quad \begin{matrix} (1a) \\ (1b) \end{matrix}$$

where $p(x, y)$ is the unknown function, $g(x, y)$ is a known source term and $k \in \mathbb{R}$ is the fixed wavenumber of the Helmholtz problem. Because of its boundary condition, it is obvious that (1) models a *cavity problem*

¹It is also possible to solve the subproblems sequentially and to exchange data after each single solve. This family of DD methods are often referred to as sweeping algorithms, and offer some advantages, notably in terms of iteration count, which will not be further discussed in this work. More details can be found for instance in [12, 13].

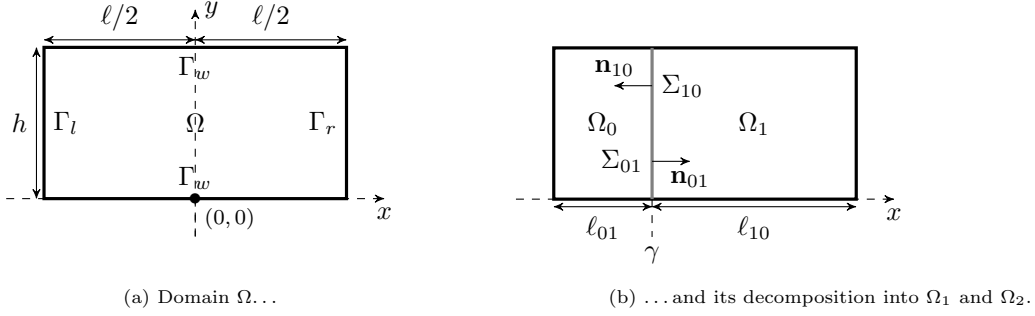


Figure 1: Reference computational domain.

exhibiting both forward- and back-propagating waves. It is important to stress that for this problem to be well-defined, we must assume that k^2 is not an eigenvalue of (1).

Let us now set up the following optimized non-overlapping Schwarz iterative scheme, indexed by n , to solve the cavity Helmholtz problem (1):

$$\left\{ \begin{array}{ll}
 \operatorname{div} \mathbf{grad} p_0^{n+1} + k^2 p_0^{n+1} = g & \text{on } \Omega_0, & (2a) \\
 +\mathbf{n}_{01} \cdot \mathbf{grad} p_0^{n+1} + \mathcal{S}_{01}(p_0^{n+1}) = +\mathbf{n}_{01} \cdot \mathbf{grad} p_1^n + \mathcal{S}_{01}(p_1^n) & \text{on } \Sigma_{01}, & (2b) \\
 p_0^{n+1} = 0 & \text{on } \Gamma, & (2c) \\
 \\
 \operatorname{div} \mathbf{grad} p_1^{n+1} + k^2 p_1^{n+1} = g & \text{on } \Omega_1, & (2d) \\
 -\mathbf{n}_{01} \cdot \mathbf{grad} p_1^{n+1} + \mathcal{S}_{10}(p_1^{n+1}) = -\mathbf{n}_{01} \cdot \mathbf{grad} p_0^n + \mathcal{S}_{10}(p_0^n) & \text{on } \Sigma_{10}, & (2e) \\
 p_1^{n+1} = 0 & \text{on } \Gamma, & (2f)
 \end{array} \right.$$

where \mathcal{S}_{ij} is the transmission operator of the optimized Schwarz algorithm at Σ_{ij} and $p_i^n(x, y)$ is the solution at iteration n on domain Ω_i . Let us stress that, since the subdomains do not overlap, the following holds true: $\mathbf{n}_{01} = -\mathbf{n}_{10}$. Once the Schwarz algorithm has converged, the solution $p(x, y)$ of the original problem (1) is recovered by concatenating the solutions $p_0(x, y)$ and $p_1(x, y)$.

In practice, let us note that the above fixed-point scheme is usually recast into the linear system [14]:

$$(\mathcal{I} - \mathcal{A})\mathbf{d} = \mathbf{b}, \quad (3)$$

where one application of the operator \mathcal{A} amounts to one iteration of the fixed-point method with *homogeneous* Dirichlet boundary conditions, where \mathcal{I} is the identity operator, where \mathbf{d} concatenates all $\mathbf{n} \cdot \mathbf{grad} p + \mathcal{S}(p)$ at the interface between the subdomains and where the right hand side vector \mathbf{b} results from the *non-homogeneous* Dirichlet boundary conditions. This linear system can then be solved with a matrix-free Krylov subspace method such as GMRES.

3. Optimal transmission operator for the rectangular cavity problem with homogeneous Dirichlet boundary conditions

In this section, we will first determine the optimal transmission operators at Σ_{01} and Σ_{10} of the Schwarz scheme (2) involving the *non-overlapping* subdomains in Figure 1b. While this work focuses on non-overlapping decompositions, the impact of an overlap on the optimal transmission operator is also discussed in this section.

3.1. Non-overlapping case

In order to further simplify the problem at hand, let us now assume that the source term g is zero. Obviously, by not imposing a source in our problem the solution $p(x, y)$ is trivially $p = 0$ since k is not an eigenvalue. This however does not jeopardize the generality of the results derived in this section.

Let us start by taking the sine Fourier series of $p_i^n(x, y)$ along the y -axis:

$$p_i^n(x, y) = \sum_{s \in \mathbb{S}} \widehat{p}_i^n(x, s) \sin(sy), \quad (4)$$

where the functions $\widehat{p}_i^n(x, s)$ are the Fourier coefficients and where s is the Fourier variable, whose values are restricted to the set

$$\mathbb{S} = \left\{ s \in \mathbb{R} \mid s = m \frac{\pi}{h}, \forall m \in \mathbb{N}_0 \right\}. \quad (5)$$

Indeed, by restricting s to the set \mathbb{S} , the boundary conditions

$$\begin{cases} p_i^n(x, 0) = 0 & \forall x \in \left[-\frac{\ell}{2}, +\frac{\ell}{2} \right], \\ p_i^n(x, h) = 0 & \forall x \in \left[-\frac{\ell}{2}, +\frac{\ell}{2} \right], \end{cases}$$

are automatically satisfied. Then, by exploiting decomposition (4), the partial differential equation (2) becomes the following ordinary differential equation:

$$\left\{ \begin{array}{ll} \frac{\partial^2 \widehat{p}_0^{n+1}}{\partial x^2} + (k^2 - s^2) \widehat{p}_0^{n+1} = 0 & \forall x \in \left[-\frac{\ell}{2}, \gamma \right] \text{ and } \forall s \in \mathbb{S}, \quad (6a) \\ + \frac{\partial \widehat{p}_0^{n+1}}{\partial x} + \lambda_{01} \widehat{p}_0^{n+1} = + \frac{\partial \widehat{p}_1^n}{\partial x} + \lambda_{01} \widehat{p}_1^n & \text{on } x = \gamma \text{ and } \forall s \in \mathbb{S}, \quad (6b) \\ \widehat{p}_0^{n+1} = 0 & \text{on } x = -\frac{\ell}{2} \text{ and } \forall s \in \mathbb{S}, \quad (6c) \\ \frac{\partial^2 \widehat{p}_1^{n+1}}{\partial x^2} + (k^2 - s^2) \widehat{p}_1^{n+1} = 0 & \forall x \in \left[\gamma, +\frac{\ell}{2} \right] \text{ and } \forall s \in \mathbb{S}, \quad (6d) \\ - \frac{\partial \widehat{p}_1^{n+1}}{\partial x} + \lambda_{10} \widehat{p}_1^{n+1} = - \frac{\partial \widehat{p}_0^n}{\partial x} + \lambda_{10} \widehat{p}_0^n & \text{on } x = \gamma \text{ and } \forall s \in \mathbb{S}, \quad (6e) \\ \widehat{p}_1^{n+1} = 0 & \text{on } x = +\frac{\ell}{2} \text{ and } \forall s \in \mathbb{S}, \quad (6f) \end{array} \right.$$

where λ_{ij} is the Fourier symbol of \mathcal{S}_{ij} . Furthermore, and for simplicity, let us define $P_i^n(s)$ as:

$$P_i^n(s) = \widehat{p}_i^n(0, s). \quad (7)$$

In order to find the best symbol λ_{ij} , we need to determine the convergence radius of the iterative scheme (6). This objective can be achieved by following the strategy discussed in [10], which can be summarized as follows.

1. Determine the solutions of (6a) and (6d) with the boundary conditions (6c) and (6f) and the definition (7).
2. Compute $\frac{\partial \widehat{p}_i^n(x, s)}{\partial x}$ at $x = \gamma$ from the solutions $\widehat{p}_i^n(x, s)$ found in the previous step.
3. The convergence radius is obtained by simplifying the transmission conditions (6b) and (6e) with the expressions found above.

By following this approach, it can be shown (see Appendix A) that the convergence radius ρ of (6) satisfies²:

$$\rho^2(s) = \frac{\lambda_{01}(s) - \lambda_{01}^{c, \text{dtn}}(s) \lambda_{10}(s) - \lambda_{10}^{c, \text{dtn}}(s)}{\lambda_{01}(s) + \lambda_{10}^{c, \text{dtn}}(s) \lambda_{10}(s) + \lambda_{01}^{c, \text{dtn}}(s)} = \frac{n_{01}(s) n_{10}(s)}{d_{01}(s) d_{10}(s)}, \quad (8)$$

where

$$\lambda_{ij}^{c, \text{dtn}}(s) = \begin{cases} \sqrt{k^2 - s^2} \cot[\ell_{ji} \sqrt{k^2 - s^2}] & \text{if } s^2 < k^2, \\ 1/\ell_{ji} & \text{if } s^2 = k^2, \\ \sqrt{s^2 - k^2} \coth[\ell_{ji} \sqrt{s^2 - k^2}] & \text{if } s^2 > k^2. \end{cases} \quad (9a)$$

$$\lambda_{ij}^{c, \text{dtn}}(s) = \begin{cases} 1/\ell_{ji} & \text{if } s^2 = k^2, \end{cases} \quad (9b)$$

$$\lambda_{ij}^{c, \text{dtn}}(s) = \begin{cases} \sqrt{s^2 - k^2} \coth[\ell_{ji} \sqrt{s^2 - k^2}] & \text{if } s^2 > k^2. \end{cases} \quad (9c)$$

The best transmission operator $\mathcal{S}_{ij}^{c, \text{dtn}}$, that is the Dirichlet-to-Neumann map, is thus

$$\mathcal{S}_{ij}^{c, \text{dtn}} = \text{Op} \left\{ \lambda_{ij}^{c, \text{dtn}} \right\}. \quad (10)$$

3.2. Overlapping case

Let us now assume a partitioning of the domain in Figure 1a into two overlapping rectangles, as shown in Figure 2. As suggested by this figure, we define ℓ_{01} (resp. ℓ_{10}) as the length of Ω_0 (resp. Ω_1) including the overlap and ℓ'_{01} (resp. ℓ'_{10}) as the length of Ω_0 (resp. Ω_1) without the overlap. By following the same strategy as in the non-overlapping case, but taking into account that Σ_{01} and Σ_{10} have now *different* locations, the convergence radius ρ^{overlap} of the overlapping variant of (6) reads (see Appendix B):

$$(\rho^{\text{overlap}})^2 = \begin{cases} \left(\frac{\lambda_{01} - \alpha \cot(\alpha \ell'_{10})}{\lambda_{01} + \alpha \cot(\alpha \ell_{01})} \frac{\lambda_{10} - \alpha \cot(\alpha \ell'_{01})}{\lambda_{10} + \alpha \cot(\alpha \ell_{10})} \right) \left(\frac{\sin(\alpha \ell'_{10}) \sin(\alpha \ell'_{01})}{\sin(\alpha \ell_{10}) \sin(\alpha \ell_{01})} \right) & \text{if } s^2 < k^2, \\ \left(\frac{\lambda_{01} - (\ell'_{10})^{-1}}{\lambda_{01} + (\ell_{01})^{-1}} \frac{\lambda_{10} - (\ell'_{01})^{-1}}{\lambda_{10} + (\ell_{10})^{-1}} \right) \left(\frac{\ell'_{10} \ell'_{01}}{\ell_{10} \ell_{01}} \right) & \text{if } s^2 = k^2, \\ \left(\frac{\lambda_{01} - \alpha \coth(\alpha \ell'_{10})}{\lambda_{01} + \alpha \coth(\alpha \ell_{01})} \frac{\lambda_{10} - \alpha \coth(\alpha \ell'_{01})}{\lambda_{10} + \alpha \coth(\alpha \ell_{10})} \right) \left(\frac{\sinh(\alpha \ell'_{10}) \sinh(\alpha \ell'_{01})}{\sinh(\alpha \ell_{10}) \sinh(\alpha \ell_{01})} \right) & \text{if } s^2 > k^2, \end{cases} \quad (11a)$$

$$\left(\frac{\lambda_{01} - (\ell'_{10})^{-1}}{\lambda_{01} + (\ell_{01})^{-1}} \frac{\lambda_{10} - (\ell'_{01})^{-1}}{\lambda_{10} + (\ell_{10})^{-1}} \right) \left(\frac{\ell'_{10} \ell'_{01}}{\ell_{10} \ell_{01}} \right) & \text{if } s^2 = k^2, \quad (11b)$$

$$\left(\frac{\lambda_{01} - \alpha \coth(\alpha \ell'_{10})}{\lambda_{01} + \alpha \coth(\alpha \ell_{01})} \frac{\lambda_{10} - \alpha \coth(\alpha \ell'_{01})}{\lambda_{10} + \alpha \coth(\alpha \ell_{10})} \right) \left(\frac{\sinh(\alpha \ell'_{10}) \sinh(\alpha \ell'_{01})}{\sinh(\alpha \ell_{10}) \sinh(\alpha \ell_{01})} \right) & \text{if } s^2 > k^2, \quad (11c)$$

where

$$\alpha(s) = \begin{cases} -j\sqrt{k^2 - s^2} & \text{if } s^2 < k^2, \\ 0 & \text{if } s^2 = k^2, \\ \sqrt{s^2 - k^2} & \text{if } s^2 > k^2. \end{cases} \quad (12a)$$

$$\alpha(s) = \begin{cases} 0 & \text{if } s^2 = k^2, \end{cases} \quad (12b)$$

$$\alpha(s) = \begin{cases} \sqrt{s^2 - k^2} & \text{if } s^2 > k^2. \end{cases} \quad (12c)$$

A few conclusions can be drawn from the above expressions. Firstly, it is clear from (11) that the optimal transmission operator writes

$$\lambda_{ij}^{c, \text{dtn, overlap}}(s) = \begin{cases} \sqrt{k^2 - s^2} \cot[\ell'_{ji} \sqrt{k^2 - s^2}] & \text{if } s^2 < k^2, \\ 1/\ell'_{ji} & \text{if } s^2 = k^2, \\ \sqrt{s^2 - k^2} \coth[\ell'_{ji} \sqrt{s^2 - k^2}] & \text{if } s^2 > k^2, \end{cases} \quad (13a)$$

$$\lambda_{ij}^{c, \text{dtn, overlap}}(s) = \begin{cases} 1/\ell'_{ji} & \text{if } s^2 = k^2, \end{cases} \quad (13b)$$

$$\lambda_{ij}^{c, \text{dtn, overlap}}(s) = \begin{cases} \sqrt{s^2 - k^2} \coth[\ell'_{ji} \sqrt{s^2 - k^2}] & \text{if } s^2 > k^2, \end{cases} \quad (13c)$$

that is $\lambda_{ij}^{c, \text{dtn, overlap}}(s)$ is equal to $\lambda_{ij}^{c, \text{dtn}}(s)$, up to the substitution $\ell_{ji} \rightarrow \ell'_{ji}$. Secondly, it is easy to notice that when there is no overlap, it holds that $\ell_{ji} = \ell'_{ji}$ and the non-overlapping case is recovered. Thirdly and most importantly, it is obvious that an overlap does *not necessarily* improve the convergence radius ρ^{overlap} *unlike* for the unbounded case [14], since when $s^2 < k^2$ (*i.e.* propagating modes) the term involving the sin functions in (11a) exhibits poles and oscillates with respect to the size of the overlap. Nonetheless, the term with the sinh functions in (11c) introduces a damping proportional to the overlap, as in the unbounded case, but only when $s^2 > k^2$ (*i.e.* evanescent modes).

²In what follows, we distinguish the cavity and unbounded contexts with the superscripts “c” and “u” respectively.

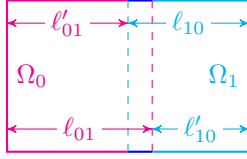


Figure 2: Overlapping partitioning of the computational domain.

4. Some local transmission operators for the cavity problem

In this section, we discuss some local transmission operators based on the Fourier symbol (9).

4.1. Zeroth-order transmission condition

A zeroth-order transmission condition (OOO^c) can easily be constructed by approximating the symbol of the DtN map with the constant term of its Taylor series expansion around $s = 0$. For the considered cavity setting, we obtain:

$$\lambda_{ij}^{c, \text{dtn}}(s) \approx \lambda_{ij}^{c, \text{oo0}}(s) = k \cot(k\ell_{ji}) \quad (14)$$

and the OOO^c transmission condition reads

$$\mathcal{S}_{ij}^{c, \text{oo0}} = k \cot(k\ell_{ji}). \quad (15)$$

As such, this operator exhibits a rather poor behavior. Indeed, the *denominator* of the convergence radius (8) involves terms of the form

$$d_{ij}(s) = \lambda_{ij}(s) + \lambda_{ji}^{c, \text{dtn}}(s), \quad (16)$$

which can *change their sign multiple times* when $s^2 < k^2$, since $\lambda_{ji}^{c, \text{dtn}}$ is nothing but a cotangent and $\lambda_{ij}^{c, \text{oo0}}$ is *constant*. Consequently, it is possible that $d_{ij} \approx 0$ for some $s \in \mathbb{S}$, leading to a very large convergence radius. In the worst case scenario, one can also have $d_{ij} = 0$ for some $s \in \mathbb{S}$ and the problem becomes ill-posed. Regularization procedures for preventing this behavior are further discussed in sections 4.4 and 4.5.

4.2. Truncated Mittag-Leffler expansion based transmission condition

In order to improve the performance of the above OOO^c transmission condition for cavity problem, we need a condition whose symbol is a better approximation of $\lambda_{ij}^{c, \text{dtn}}$. To this end, an option is to exploit the Mittag-Leffler [20] expansion of $\cot(z)$ according to its poles, leading to the following partial fraction decomposition [20]:

$$z \cot(az) = \frac{1}{a} \left(1 + 2 \sum_{n=1}^{\infty} \frac{z^2}{z^2 - \left(\frac{n\pi}{a}\right)^2} \right), \quad (17)$$

that can be exploited to expand the symbol of the DtN map as

$$\lambda_{ij}^{c, \text{dtn}}(s) = \frac{1}{\ell_{ji}} \left(1 + 2 \sum_{n=1}^{\infty} \frac{1 - \frac{s^2}{k^2}}{1 - \left(\frac{n\pi}{k\ell_{ji}}\right)^2 - \frac{s^2}{k^2}} \right). \quad (18)$$

This symbol can hence be localized by *truncating* the series up to the N^{th} term, enabling us to form a N -term truncated Mittag-Leffler expansion based (ML^c) transmission condition:

$$\mathcal{S}_{ij}^{c, \text{ml}(N)} = \frac{1}{\ell_{ji}} \left\{ 1 + 2 \sum_{n=1}^N \left[1 + \frac{\text{div } \mathbf{grad}}{k^2} \right] \left[1 - \left(\frac{n\pi}{k\ell_{ji}}\right)^2 + \frac{\text{div } \mathbf{grad}}{k^2} \right]^{-1} \right\}. \quad (19)$$

As increasing the number of terms in this expansion makes the transmission condition arbitrarily precise, the poor convergence rate of the previous OO^c operator can be alleviated. This comes however at the cost of N auxiliary computations to account for the N inverse operations appearing in (19) [11]. For this reason, it is desirable to devise an approximation of $\lambda_{ij}^{c, \text{dtn}}(s)$ with a limited number of auxiliary terms.

4.3. Padé approximant based transmission condition

A Padé rational approximation exhibits usually a good convergence rate with respect to its order $[M/N]$, where M (resp. N) denote the order of the numerator (resp. denominator). One can construct it by exploiting the continued fraction expansion of the function to approach [21]. By taking the reciprocal of the continued fraction expansion of the tangent function [22], we have:

$$z \cot(z) = 1 - \frac{z^2}{3 - \frac{z^2}{7 - \frac{z^2}{9 - \dots}}} = b_0 + \frac{a_1}{b_1 + \frac{a_2}{b_2 + \frac{a_3}{b_3 + \dots}}}, \quad (20)$$

where

$$\begin{cases} b_n = 2n + 1 & \forall n \geq 0, \\ a_n = -z^2 & \forall n \geq 1. \end{cases}$$

The Padé approximant can then be determined from the following recurrence formula [21]:

$$\frac{A_m}{B_l} = \frac{b_m A_{m-1} + a_m A_{m-2}}{b_l B_{l-1} + a_l B_{l-2}} \quad \forall m \geq 2 \text{ and } \forall l \geq 2, \quad (22)$$

with

$$\begin{cases} A_0 = b_0, \\ B_0 = 1, \end{cases} \quad \text{and} \quad \begin{cases} A_1 = b_1 b_0 + a_1, \\ B_1 = b_1. \end{cases}$$

That is, we have for the $z \cot(z)$ function:

$$\begin{cases} A_0 = 1, \\ B_0 = 1, \end{cases} \quad \text{and} \quad \begin{cases} A_1 = 3 - z^2, \\ B_1 = 3, \end{cases} \quad \text{and} \quad \begin{cases} A_m = (2m + 1)A_{m-1} - z^2 A_{m-2}, \\ B_l = (2l + 1)B_{l-1} - z^2 B_{l-2}. \end{cases} \quad (23)$$

Starting from this recurrence formula and choosing $l = m$, we can devise a N -term decomposition of the form

$$z \cot(z) \approx \frac{A_N}{B_N} = \tilde{C}_0 + \sum_{n=0}^N \frac{\tilde{A}_i}{z^2 - \tilde{B}_i}. \quad (24)$$

However, compared with the unbounded case where the coefficients of the Padé approximant of the DtN map are known analytically and exploited to construct the PADE^u operator [11], no closed form formulae were found for the coefficients \tilde{C}_0 , \tilde{A}_i and \tilde{B}_i of (24). Nevertheless, those can be computed numerically by

1. performing a polynomial long division of A_N/B_N , that is $A_N = \tilde{C}_0 B_N + R$,
2. computing the poles \tilde{B}_i of R/B_N and
3. determining the residues \tilde{A}_i of R/B_N .

The numerically demanding part of this approach is the calculation of the poles of R/B_N , *i.e.* the zeros of B_N , which requires arbitrary-precision arithmetic as the coefficients of the monomials appearing in B_N can be vary large.

In this work, this is achieved with the `MPSolve` library³ [23]. Within that framework, it takes less than 5 minutes⁴ to compute the \tilde{C}_0 , \tilde{A}_i and \tilde{B}_i coefficients in the very large case of $N = 1024$ for instance. Of course, these coefficients can be pre-computed and tabulated for various values of N and the actual transmission condition recovered with the change of variable $z = \ell_{ji} \sqrt{k^2 - s^2}$ (see paragraph below). For illustration purposes, the Padé coefficients are presented in Table 1 for $N \in [1, 4]$.

³See github.com/robot1/MPSolve.

⁴This computation was carried out with a dual-core laptop-class Intel i7-7500U CPU.

N	\tilde{C}_0	\tilde{A}_i	\tilde{B}_i	N	\tilde{C}_0	\tilde{A}_i	\tilde{B}_i
1	6.00×10^0	7.50×10^1	1.50×10^1	4	4.50×10^1	1.97×10^1	9.87×10^0
2	1.50×10^1	2.05×10^1	9.94×10^0			8.03×10^1	3.96×10^1
		1.13×10^3	9.51×10^1			4.03×10^2	1.06×10^2
3	2.80×10^1	1.97×10^1	9.87×10^0			3.02×10^4	8.35×10^2
		1.09×10^2	4.20×10^1				
		7.31×10^3	3.26×10^2				

Table 1: Padé coefficients \tilde{C}_0 , \tilde{A}_i and \tilde{B}_i for $N \in [1, 4]$.

Capitalizing on the above development, we can now devise a new approximation (PADE^c) of $\lambda_{ij}^{c, \text{dtn}}$ of the form

$$\lambda_{ij}^{c, \text{dtn}}(s) \approx \lambda_{ij}^{c, \text{pade}(N)}(s) = \frac{1}{\ell_{ji}} \left(\tilde{C}_0 + \sum_{n=1}^N \frac{\tilde{A}_n}{(k\ell_{ji})^2 \left(1 - \frac{s^2}{k^2}\right) - \tilde{B}_n} \right), \quad (25)$$

by exploiting the change of variable $z = \ell_{ji}\sqrt{k^2 - s^2}$. The operator associated with this symbol then reads:

$$\mathcal{S}_{ij}^{c, \text{pade}(N)} = \frac{1}{\ell_{ji}} \left\{ \tilde{C}_0 + \sum_{n=1}^N \tilde{A}_n \left[\left(k\ell_{ji} \right)^2 \left(1 + \frac{\text{div grad}}{k^2} \right) - \tilde{B}_n \right]^{-1} \right\}. \quad (26)$$

4.4. Regularization with a constant imaginary part

As already mentioned earlier, the zeroth-order transmission condition optimized for the cavity problem can lead to an ill-posed problem when one of the $d_{ij}(s)$ terms in the denominator of the convergence radius (8) equals (or is sufficiently close to) zero. This problem is however not peculiar to the OO0^c condition and affects the ML^c and PADE^c ones as well, requiring therefore a regularization procedure.

The most straightforward and simple strategy to regularize the OO0^c, ML^c and PADE^c conditions is to exploit the fact that those operators are purely real-valued. Consequently, by adding a purely imaginary part, the $d_{ij}(s)$ terms can be pushed away from zero and the convergence radius $\rho(s)$ can be guaranteed to be well defined. Formally, the regularized OO0^c, ML^c and PADE^c operators read⁵

$$\mathcal{S}_{ij}^{c, \text{oo0/ml}(N)/\text{pade}(N), \text{r}(\chi)} = \mathcal{S}_{ij}^{c, \text{oo0/ml}(N)/\text{pade}(N)} + \mathcal{J}\chi k, \quad (27)$$

where $\chi \in \mathbb{R}$ is the regularization parameter. Numerical experiments showing the impact of this regularization approach are further discussed in sections 7 and 8.

4.5. Regularization by mixing operators optimized for cavity and unbounded problems

The above regularization is in some sense suboptimal as it acts on all $s \in \mathbb{S}$, while regularization is required only in the $s^2 < k^2$ case. A more selective approach can be achieved by realizing that the PADE^u operator exhibits the following properties [24]:

1. it is approximately imaginary when $s^2 < k^2$,
2. it is approximately real when $s^2 > k^2$ and
3. it is a good approximation of the DtN map when $s^2 > k^2$ (see discussion in section 6),

⁵We use the superscript “r(χ)” to denote the regularization with a constant imaginary part proportional to χ.

when N is sufficiently high and with an appropriate rotation of the branch cut of the square-root operator [24]. Therefore, a regularized operator can be constructed by combining either the OO^c , the ML^c or the PADE^c operator with the PADE^u one in a convex way. These new operators will be further referred to as *mixed* operator and write⁶

$$\mathcal{S}_{ij}^{m(\varepsilon, M), \text{oo}0/\text{ml}(N)/\text{pade}(N)} = \varepsilon \mathcal{S}_{ij}^{c, \text{oo}0/\text{ml}(N)/\text{pade}(N)} + (1 - \varepsilon) \mathcal{S}_{ij}^{u, \text{pade}(M)}, \quad (28)$$

where $\varepsilon \in]0, 1[$ denotes the regularization parameter of the mixed formulation.

4.6. Estimate for the minimum number of auxiliary unknowns

Given the ML^c and PADE^c transmission condition, one question naturally arise: how many auxiliary terms should be selected? In order to answer this question, one could opt for the following criterion: the number of auxiliary terms N should at least be equal to the number of poles of $\lambda_{ij}^{c, \text{dtn}}$, as it seems legitimate to assume that the behavior of $\lambda_{ij}^{c, \text{dtn}}$ is driven by its poles in the range $s^2 < k^2$.

Given the Mittag-Leffler expansion of $\lambda_{ij}^{c, \text{dtn}}$, it is clear that the poles must satisfy

$$s^2 = k^2 - \left(\frac{n\pi}{\ell_{ij}} \right)^2 \quad \forall n > 0, \quad (29)$$

which implies that

$$k^2 - \left(\frac{n\pi}{\ell_{ij}} \right)^2 > 0 \quad (30)$$

and thus

$$0 < n < 2 \frac{\ell_{ij}}{\lambda_w}, \quad (31)$$

since k , n and ℓ_{ij} are positive by construction and where $\lambda_w = 2\pi/k$ is the wavelength.

Therefore, according to the pole criterion stated above, the minimum number of terms N_{\min}^{poles} for localizing $\lambda_{ij}^{c, \text{dtn}}$ is

$$N_{\min}^{\text{pole}} = \left\lceil 2 \frac{\ell_{ij}}{\lambda_w} \right\rceil \quad (32)$$

and depends on the size of the subdomains and on the wavelength. As discussed further in section 7.3, this criterion seems however pessimistic, as lower values of N_{\min}^{pole} provide already acceptable results.

5. Generalizations

The transmission operators detailed in the pervious section are restricted to the very particular case of a cavity with *Dirichlet* boundary conditions divided into *two* subdomains. In order to generalize this setting, we discuss in section the cases of many subdomains in a one-dimensional partitioning and of Neumann boundary conditions.

5.1. One-dimensional partitioning with more than two subdomains

Let us start with the one-dimensional partitioning of the computational domain into D subdomains, as shown in Figure 3a. In such a one-dimensional domain decomposition, the physical meaning of the ℓ_{ji} coefficient appearing in $\lambda_{ij}^{c, \text{dtn}}(s)$ must be clarified. In the two subdomains case, *the ℓ_{ji} coefficients represents the distance between Σ_{ij} and the reflecting wall located in the \mathbf{n}_{ij} direction*. This interpretation can be directly applied to the D subdomains case to define the ℓ_{ji} coefficients, as shown in Figure 3b for the $D = 3$ case.

⁶We use the superscript “ $m(\varepsilon, M)$ ” to denote mixed operators involving a M -term PADE^u operator with a weight of $(1 - \varepsilon)$.

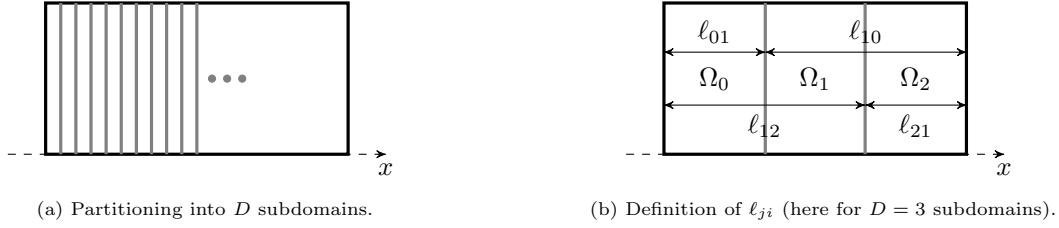


Figure 3: One-dimensional partitioning of the rectangular cavity.

5.2. Neumann boundary conditions

So far, we considered only the situation where the reflecting wall associated with \mathcal{S}_{ij} is implemented with an homogeneous Dirichlet boundary condition, *i.e.* a soft-wall condition. In the case of an homogeneous Neumann boundary condition, *i.e.* a hard-wall condition, the following DtN map is obtained:

$$\lambda_{ij}^{c, \text{dtn, neumann}}(s) = \begin{cases} -\sqrt{k^2 - s^2} \tan\left[\ell_{ji}\sqrt{k^2 - s^2}\right] & \text{if } s^2 < k^2, \\ 0 & \text{if } s^2 = k^2, \\ \sqrt{s^2 - k^2} \tanh\left[\ell_{ji}\sqrt{s^2 - k^2}\right] & \text{if } s^2 > k^2, \end{cases} \quad (33a)$$

$$\lambda_{ij}^{c, \text{dtn, neumann}}(s) = 0 \quad \text{if } s^2 = k^2, \quad (33b)$$

$$\lambda_{ij}^{c, \text{dtn, neumann}}(s) = \sqrt{s^2 - k^2} \tanh\left[\ell_{ji}\sqrt{s^2 - k^2}\right] \quad \text{if } s^2 > k^2, \quad (33c)$$

by following the same strategy as in section 3. It is worth stressing the similarities between (9) and (33). This DtN map can then be localized using the previously presented approaches and a OOO^c , ML^c or PADE^c transmission condition can be devised. In this regard, let us note that that Mittag-Leffler expansion of $\tan(z)$ reads [25]

$$z \tan(az) = -\frac{2}{a} \sum_{n=0}^{\infty} \frac{z^2}{z^2 - \left[\frac{(n+\frac{1}{2})\pi}{a}\right]^2} \quad (34)$$

and its continued fraction expansion has the following form [22]:

$$z \tan(z) = \frac{z^2}{1 - \frac{z^2}{3 - \frac{z^2}{5 - \dots}}} = b_0 + \frac{a_1}{b_1 + \frac{a_2}{b_2 + \frac{a_3}{b_3 + \dots}}} \quad (35)$$

These results are given here for the sake of completeness and will not be further discussed in this work.

6. Operators optimized for unbounded problems without obstacles in a cavity context

In this section we derive some estimates on the performance of operators optimized for unbounded problems without obstacles when used in a cavity problem. In particular, *i)* we first compare the DtN operator related to an unbounded problem without obstacles $\mathcal{S}_{ij}^{u, \text{dtn}}$ with its cavity counter part $\mathcal{S}_{ij}^{c, \text{dtn}}$, then *ii)* we discuss the convergence radius of the OS scheme when using $\mathcal{S}_{ij}^{u, \text{dtn}}$ as a transmission operator for the rectangular cavity problem (1), as well as *iii)* the particular case of the optimized order 0 operator (OOO^u) [8].

6.1. Dirichlet-to-Neumann operators

Let us consider the following Helmholtz problem without obstacles:

$$\begin{cases} \operatorname{div} \mathbf{grad} p + k^2 p = g & \text{on } \mathbb{R}^2, \\ \lim_{r \rightarrow \infty} \sqrt{r} \left(\frac{\partial p}{\partial r} - jkp \right) = 0, \end{cases} \quad (36a)$$

$$\lim_{r \rightarrow \infty} \sqrt{r} \left(\frac{\partial p}{\partial r} - jkp \right) = 0, \quad (36b)$$

where $r^2 = x^2 + y^2$. In this case, it can be shown that the optimal transmission operator $\mathcal{S}_{ij}^{\text{u, dtn}}$ for solving this problem with an OS scheme is [11]:

$$\mathcal{S}_{ij}^{\text{u, dtn}} = \text{Op}\left(\lambda_{ij}^{\text{u, dtn}}\right) = -jk\sqrt{1 + \frac{\text{div}_{\Sigma} \mathbf{grad}_{\Sigma}}{k^2}}, \quad (37)$$

where

$$\lambda_{ij}^{\text{u, dtn}} = -jk\sqrt{1 - \frac{s^2}{k^2}}. \quad (38)$$

By comparing (38) and (9), it is easy to realize that

$$\lambda_{ij}^{\text{c, dtn}}(s) - \lambda_{ij}^{\text{u, dtn}}(s) = \begin{cases} \sqrt{k^2 - s^2} \cot\left[\ell_{ji}\sqrt{k^2 - s^2}\right] + j\sqrt{k^2 - s^2} & \text{if } s^2 < k^2, \\ 1/\ell_{ji} & \text{if } s^2 = k^2, \\ \sqrt{s^2 - k^2} \coth\left[\ell_{ji}\sqrt{s^2 - k^2}\right] - \sqrt{s^2 - k^2} & \text{if } s^2 > k^2. \end{cases} \quad (39a)$$

$$\lambda_{ij}^{\text{c, dtn}}(s) - \lambda_{ij}^{\text{u, dtn}}(s) = \begin{cases} 1/\ell_{ji} & \text{if } s^2 = k^2, \end{cases} \quad (39b)$$

$$\lambda_{ij}^{\text{c, dtn}}(s) - \lambda_{ij}^{\text{u, dtn}}(s) = \begin{cases} \sqrt{s^2 - k^2} \coth\left[\ell_{ji}\sqrt{s^2 - k^2}\right] - \sqrt{s^2 - k^2} & \text{if } s^2 > k^2. \end{cases} \quad (39c)$$

Interestingly, by exploiting the definition of the hyperbolic cotangent [22], the case $s^2 > k^2$ can be further simplified into

$$\begin{aligned} \lambda_{ij}^{\text{c, dtn}}(s) - \lambda_{ij}^{\text{u, dtn}}(s) &= \sqrt{s^2 - k^2} \coth\left[\ell_{ji}\sqrt{s^2 - k^2}\right] - \sqrt{s^2 - k^2} \\ &= \sqrt{s^2 - k^2} \left(\frac{\exp\left(2\ell_{ji}\sqrt{s^2 - k^2}\right) + 1}{\exp\left(2\ell_{ji}\sqrt{s^2 - k^2}\right) - 1} - 1 \right) \\ &= \frac{2}{\exp\left(2\ell_{ji}\sqrt{s^2 - k^2}\right) - 1} \sqrt{s^2 - k^2} \quad \text{if } s^2 > k^2, \end{aligned} \quad (40)$$

which yields:

$$\lim_{s \rightarrow \infty} \lambda_{ij}^{\text{c, dtn}}(s) - \lambda_{ij}^{\text{u, dtn}}(s) = 0. \quad (41)$$

In other words, for the case $s^2 > k^2$, the symbol $\lambda_{ij}^{\text{u, dtn}}(s)$ is converging towards $\lambda_{ij}^{\text{c, dtn}}(s)$ as s grows. Furthermore, as the difference between both symbols is decreasing exponentially, $\lambda_{ij}^{\text{u, dtn}}(s)$ is an excellent approximation of $\lambda_{ij}^{\text{c, dtn}}(s)$ when $s^2 > k^2$.

Regarding the case $s^2 < k^2$, as the codomains of $\lambda_{ij}^{\text{u, dtn}}(s)$ (which is purely imaginary) and $\lambda_{ij}^{\text{c, dtn}}(s)$ (which is purely real) do not match, the expression in (39a) cannot be further simplified. For illustration purposes, the graphs of $\lambda_{ij}^{\text{u, dtn}}$ and $\lambda_{ij}^{\text{c, dtn}}$ are depicted in Figure 4 for different values of k (\Re and \Im are respectively denoting the real and imaginary part functions).

6.2. Best convergence radius

We already know from the previous section that $\lambda_{ij}^{\text{u, dtn}}(s)$ is a good approximation of $\lambda_{ij}^{\text{c, dtn}}(s)$ when $s^2 > k^2$, that is for *evanescent modes*. For this reason, local approximations of $\lambda_{ij}^{\text{u, dtn}}$ are legitimate, yet suboptimal, candidates for approximating $\lambda_{ij}^{\text{c, dtn}}$.

In terms of convergence radius, as defined in (8), it is easy to show that

$$\rho^2(s) = \begin{cases} \frac{j - \cot\left[\ell_{ji}\sqrt{k^2 - s^2}\right]}{j + \cot\left[\ell_{ji}\sqrt{k^2 - s^2}\right]} \frac{j - \cot\left[\ell_{ij}\sqrt{k^2 - s^2}\right]}{j + \cot\left[\ell_{ij}\sqrt{k^2 - s^2}\right]} & \text{if } s^2 < k^2, \\ 1 & \text{if } s^2 = k^2, \\ \frac{1 - \coth\left[\ell_{ji}\sqrt{s^2 - k^2}\right]}{1 + \coth\left[\ell_{ji}\sqrt{s^2 - k^2}\right]} \frac{1 - \coth\left[\ell_{ij}\sqrt{s^2 - k^2}\right]}{1 + \coth\left[\ell_{ij}\sqrt{s^2 - k^2}\right]} & \text{if } s^2 > k^2, \end{cases} \quad (42a)$$

$$\rho^2(s) = \begin{cases} 1 & \text{if } s^2 = k^2, \end{cases} \quad (42b)$$

$$\rho^2(s) = \begin{cases} \frac{1 - \coth\left[\ell_{ji}\sqrt{s^2 - k^2}\right]}{1 + \coth\left[\ell_{ji}\sqrt{s^2 - k^2}\right]} \frac{1 - \coth\left[\ell_{ij}\sqrt{s^2 - k^2}\right]}{1 + \coth\left[\ell_{ij}\sqrt{s^2 - k^2}\right]} & \text{if } s^2 > k^2, \end{cases} \quad (42c)$$

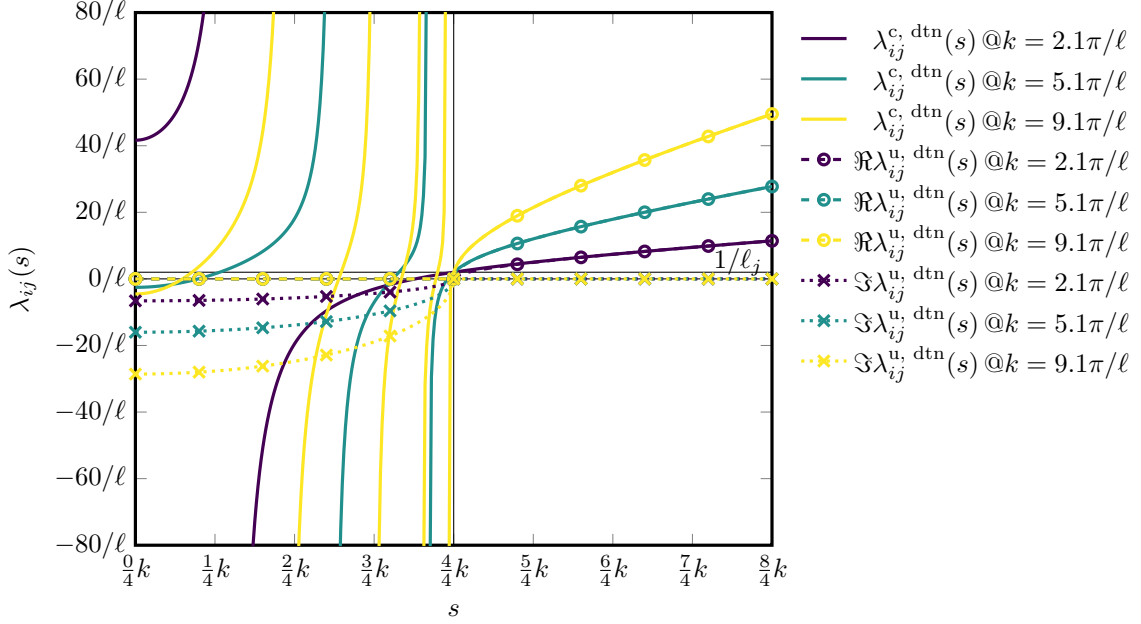


Figure 4: Graphs of $\lambda_{ij}^{u, dttn}(s)$ and $\lambda_{ij}^{c, dttn}(s)$ for different values of k .

and

$$|\rho(s)| = \begin{cases} 1 & \text{if } s^2 \leq k^2, \\ \exp(-\ell\sqrt{s^2 - k^2}) & \text{if } s^2 > k^2, \end{cases} \quad (43a)$$

$$|\rho(s)| = \begin{cases} 1 & \text{if } s^2 \leq k^2, \\ \exp(-\ell\sqrt{s^2 - k^2}) & \text{if } s^2 > k^2, \end{cases} \quad (43b)$$

when $\lambda_{ij}^{c, dttn}$ is approximated with $\lambda_{ij}^{u, dttn}$. For this reason, the transmission operators that are good approximations of $\lambda_{ij}^{u, dttn}$, such that the optimized order 2 (OO2^u) [10] or the N -term Padé-localized (PADE^u) [11] operators, should exhibit a convergence radius close to (43). In other words, those local operators should exhibit a slow convergence for the *propagating modes* ($s^2 < k^2$) and a fast convergence for the *evanescent* ones ($s^2 > k^2$).

6.3. Particular case of the optimized order 0 operator

Before concluding this subsection, it is worth mentioning that in the case of the OO0^u operator, we have that $\lambda_{ij}^{u, oo0} = -jk$ and therefore

$$|\rho(s)| = 1. \quad (44)$$

7. Numerical validation and comparison between the different operators

In this section we analyze the performance of the different transmission conditions developed in section 4 and compare them with the operators of section 6. To this end, we consider the rectangular cavity shown in Figure 1a and solve the time-harmonic Helmholtz equation over Ω with the following boundary conditions imposed on Γ :

$$\begin{cases} p = 0 & \text{on } \Gamma_w \cup \Gamma_r, \end{cases} \quad (45a)$$

$$\begin{cases} p = \sum_{m=1}^K \sin\left(m\frac{\pi}{h}y\right) & \text{on } \Gamma_l, \end{cases} \quad (45b)$$

where K designates the number of modes used to excite the cavity. This Helmholtz problem is then decomposed into D subdomains of equal size and solved with an optimized Schwarz scheme combined with a GMRES algorithm *without restart*. Let us mention as well that the software implementation relies on the GmshDDM and GmshFEM [26] frameworks⁷ and exploits a finite element (FE) discretization of the subproblems. In the case of the $\mathcal{S}_{ij}^{c, \text{pade}(N)}$ and $\mathcal{S}_{ij}^{c, \text{ml}(N)}$ operators, the FE variational formulations involve auxiliary unknowns for the treatment of the inverse operation, as proposed in [11]. However, let us note that since the new transmission operators are not symmetric, *i.e.* $\mathcal{S}_{ij}^{c, \text{oo0/ml}(N)/\text{pade}(N)} \neq \mathcal{S}_{ji}^{c, \text{oo0/ml}(N)/\text{pade}(N)}$, the amount of auxiliary fields must be doubled. The linear solvers are taken from the PETSc [27] and MUMPS [28] libraries.

Unless stated otherwise, the cavity has an aspect ratio of $\ell/h = 2$ and a length-to-wavelength ratio of $\ell/\lambda_w = \frac{157.085}{2\pi} \approx 25.001$. This configuration allows 25 non-evanescent modes and is excited with the $K = 50$ first modes. The geometry is discretized with a mesh consisting of 8 triangular elements per wavelength and the subproblems are discretized with an FE method of order 4. The stopping criterion of the GMRES solver is set to a relative tolerance decrease of $\|\mathbf{r}_i\|/\|\mathbf{r}_0\| = 10^{-6}$, where \mathbf{r}_i is the residual vector at iteration i and \mathbf{r}_0 is the residual vector of the first guess, which was chosen equal to zero.

7.1. Two subdomains case

Let us start by studying the performance of the transmission conditions developed in section 4 when applied to a rectangular cavity divided into two subdomains. The convergence history of the GMRES solver is shown in Figure 5. From these data, it is clear that all transmission conditions converge, with the exception of $\mathcal{S}_{ij}^{c, \text{oo0}}$ that stagnates after approximately 100 iterations. In addition, it appears clearly that $\mathcal{S}_{ij}^{c, \text{ml}(32)}$ and $\mathcal{S}_{ij}^{c, \text{pade}(32)}$ outperform the transmission conditions devised for unbounded problems. Furthermore, the best operator in this numerical experiment is $\mathcal{S}_{ij}^{c, \text{pade}(32)}$ that converges without any noticeable plateau.

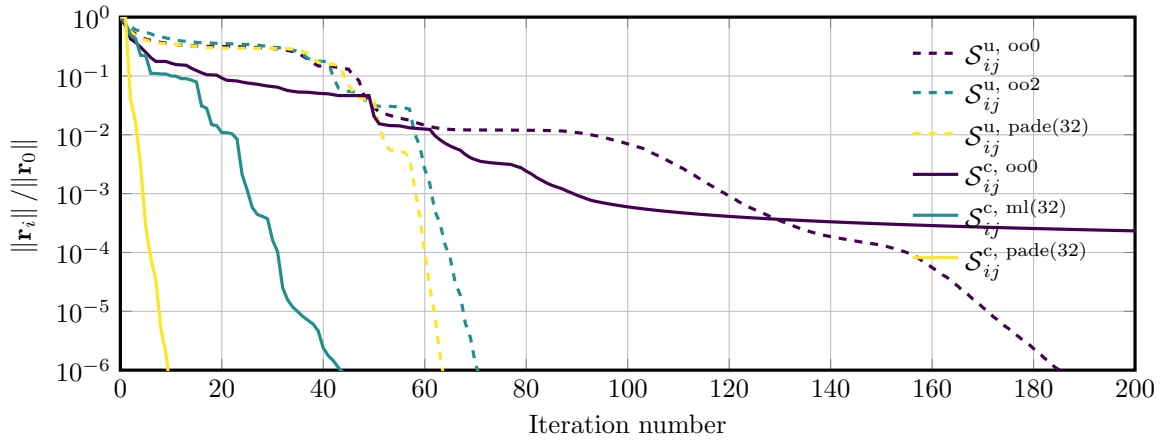


Figure 5: Convergence history of the GMRES solver – rectangular cavity with $D = 2$ subdomains.

As the closed form solution p_{CF} of this canonical problem is known, *i.e.*

$$p_{\text{CF}} = \sum_{m=1}^K \frac{\sin [k_x(m)(\ell - x)]}{\sin [k_x(m)\ell]} \sin [k_y(m)] \quad (46)$$

with

$$k_y(m) = m \frac{\pi}{h} \quad \text{and} \quad k_x(m) = \sqrt{k^2 - k_y^2(m)}, \quad (47)$$

⁷See git.rwth-aachen.de/marsic/closeddm, gitlab.onelab.info/gmsh/ddm and gitlab.onelab.info/gmsh/fem.

let us determine the accuracy of the above simulations by computing the relative L_2 error \mathcal{E} between the FE solution p_{FE} and p_{CF} :

$$\mathcal{E} = \sqrt{\frac{\int_{\Omega} |p_{\text{CF}} - p_{\text{FE}}|^2 d\Omega}{\int_{\Omega} |p_{\text{CF}}|^2 d\Omega}}, \quad (48)$$

where the above integrals are evaluated using a quadrature rule with twice the amount of integration points than the number used for the FE computations. The L_2 errors associated with the different OS schemes of Figure 5 are gathered in Table 2 together with the error associated with the MUMPS direct solver. These data show clearly that all transmission conditions and the direct solver lead to errors of the same order of magnitude.

$\mathcal{S}_{ij}^{\text{u}, \text{oo0}}$	$\mathcal{S}_{ij}^{\text{u}, \text{oo2}}$	$\mathcal{S}_{ij}^{\text{u}, \text{pade}(32)}$	$\mathcal{S}_{ij}^{\text{c}, \text{oo0}}$	$\mathcal{S}_{ij}^{\text{c}, \text{ml}(32)}$	$\mathcal{S}_{ij}^{\text{c}, \text{pade}(32)}$	MUMPS
1.73×10^{-4}	1.73×10^{-4}	1.77×10^{-4}	DNC	1.81×10^{-4}	2.41×10^{-4}	1.78×10^{-4}

Table 2: Relative L_2 errors \mathcal{E} – rectangular cavity with $D = 2$ subdomains (“DNC” stands for “did not converge”).

Let us now focus on the wall-clock time required to complete the above computations⁸, as reported in Table 3. In order to analyze these values, let us stress that they heavily depend on the actual software implementation of the FE and OS tools. Nonetheless, some general remarks can be drawn.

1. The OO0^{u} and OO2^{u} operators are the computationally cheapest to apply, as they do not involve auxiliary unknowns.
2. The ML^{c} and PADE^{c} operators are computationally more expensive than PADE^{u} , since they require two sets of auxiliary unknowns as they are not symmetric, *i.e.* $\mathcal{S}_{ij}^{\text{c}, \text{ml}(N)/\text{pade}(N)} \neq \mathcal{S}_{ji}^{\text{c}, \text{ml}(N)/\text{pade}(N)}$.
3. The regularization procedure involving PADE^{u} further increases the computational cost, as additional auxiliary unknowns are introduced.

In the current software implementation, the subproblems are solved with the direct solver MUMPS and the resulting LU factorization is reused in the subsequent OS iterations. Therefore, the first iteration is more time consuming than the other ones and the data in Table 3 are thus split in different subquantities. By defining T_i as the share of the total wall clock time T_{tot} dedicated to the i^{th} iteration, *i.e.* $T_{\text{tot}} = \sum_{i=1}^I T_i$ with I the total number of GMRES iterations required for convergence, we report in Table 3 the following values: T_{tot} , T_1 , $\overline{T_{2,I}}$, where $\overline{T_{i,j}}$ is the mean value of the sequence $[T_i, \dots, T_j]$, and I .

Quantity of interest	$\mathcal{S}_{ij}^{\text{u}, \text{oo0}}$	$\mathcal{S}_{ij}^{\text{u}, \text{oo2}}$	$\mathcal{S}_{ij}^{\text{u}, \text{pade}(32)}$	$\mathcal{S}_{ij}^{\text{c}, \text{oo0}}$	$\mathcal{S}_{ij}^{\text{c}, \text{ml}(32)}$	$\mathcal{S}_{ij}^{\text{c}, \text{pade}(32)}$	Unit
T_{tot}	123	52	51	DNC	45	18	s
T_1	9.66	9.64	10.39	DNC	11.20	11.17	s
$\overline{T_{2,I}}$	0.61	0.61	0.64	DNC	0.78	0.75	s
I	186	71	64	DNC	44	10	-

Table 3: Wall-clock times – rectangular cavity with $D = 2$ subdomains (T_i is the share of the total wall-clock time, in seconds, taken by the i^{th} iteration, I is the total number of GMRES iterations, $\overline{T_{i,j}}$ is the mean value of the sequence $[T_i, \dots, T_j]$ and “DNC” stands for “did not converge”).

⁸Those calculations were carried out with an eight-core desktop-class Intel Xeon E5-2630 CPU and parallelized with two processes with 4 threads each.

From the data gathered in Table 3, it is clear that $\mathcal{S}_{ij}^{c, \text{pade}(32)}$ leads to both the minimal amount of iterations and the fastest computation with respect to the wall clock time. Nonetheless, it is evident that the cost of T_1 and $\overline{T_{2,I}}$ is higher for $\mathcal{S}_{ij}^{c, \text{pade}(32)}$ and $\mathcal{S}_{ij}^{c, \text{ml}(32)}$ than for the other transmission operators, in accordance with the remarks drawn above. The novel operators will therefore lead to the fastest computations only when the reduction of the iteration count is sufficiently high, when compared with the transmission conditions optimized for unbounded problems (see related discussion in sections 9).

7.2. Regularized and mixed transmission conditions

As discussed in sections 4.4 and 4.5, a regularization term or a mixed transmission condition can be used to prevent the convergence radius from becoming very large (or, in the worst case, ill-defined). The performance of those transmission conditions is shown in Figures 6a and 6b for $\mathcal{S}_{ij}^{c, \text{oo0}, r(\chi)}$ and $\mathcal{S}_{ij}^{m(\varepsilon, M), \text{oo0}}$ respectively with $D = 8$ subdomains. It is clear in the figures that regularizing the OO0^c operator by adding an imaginary part (resp. mixing it with PADE^u) improves the OO0^c condition, as long as this regularization is large (resp. small) enough. Nonetheless, this does not lead to any improvement with respect to the original OO0^u or PADE^u conditions.

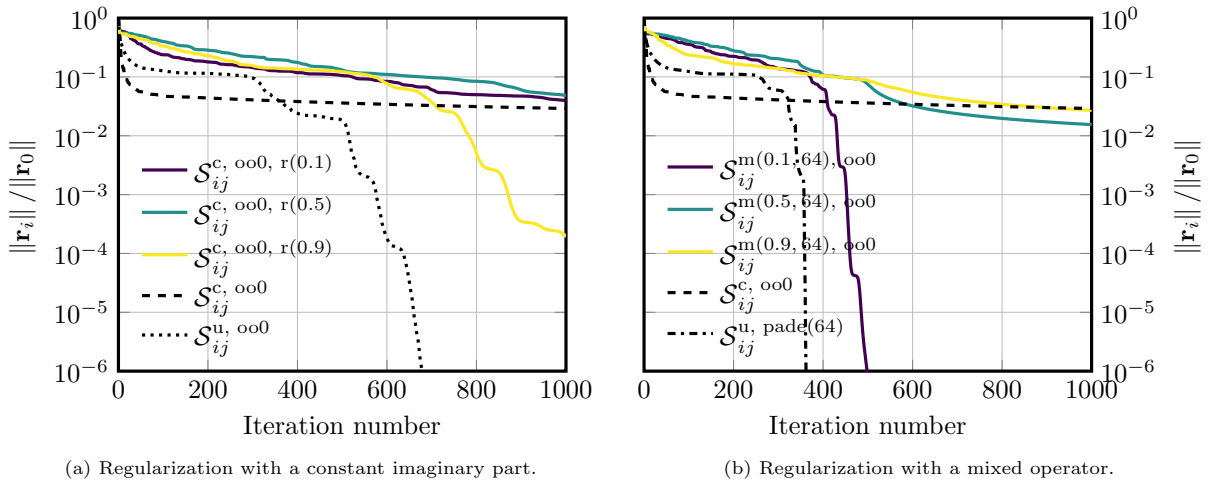
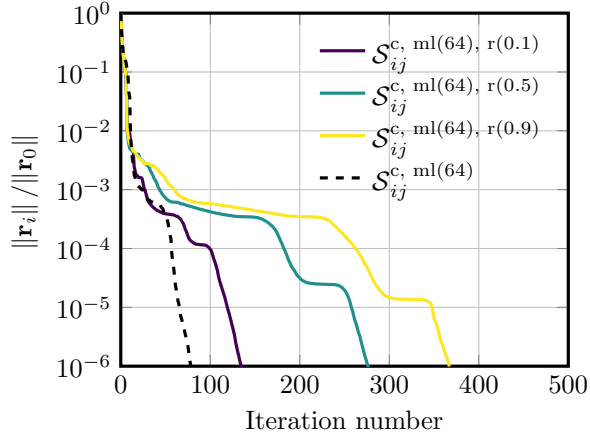


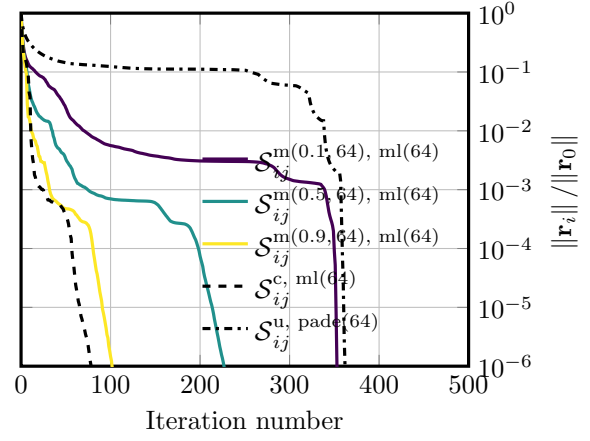
Figure 6: Regularized and mixed OO0^c – rectangular cavity with $D = 8$ subdomains.

A similar numerical experiment can also be carried out for the regularization of the ML^c condition. From the GMRES convergence histories depicted in Figure 7, it can be noticed that while the performance of ML^c remains better than PADE^u , the regularization increases the number of iterations required to reach convergence. Nonetheless, this increase declines as the regularization becomes lighter, *i.e.* when χ (resp. ε) becomes small (resp. large).

An analogous numerical experiment is performed once more for the regularization of the PADE^c condition. This last scenario shows a behavior similar to ML^c , as it can be directly observed in Figure 8.

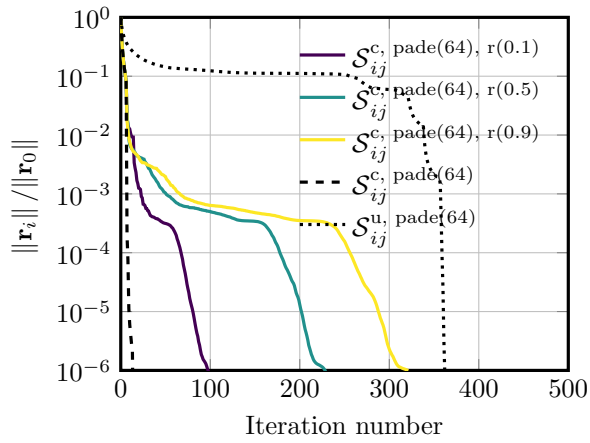


(a) Regularization with a constant imaginary part.

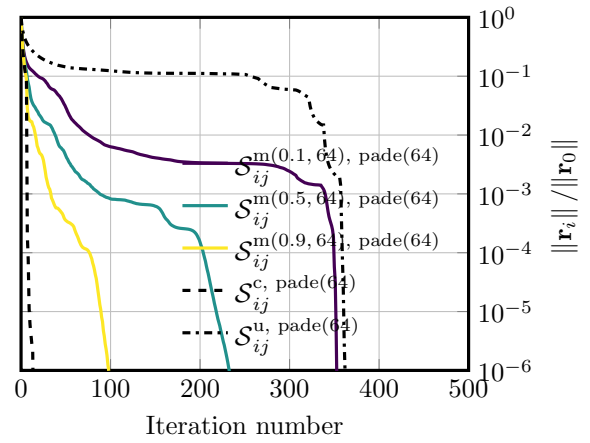


(b) Regularization with a mixed operator.

Figure 7: Regularized and mixed ML^c – rectangular cavity with $D = 8$ subdomains.



(a) Regularization with a constant imaginary part.

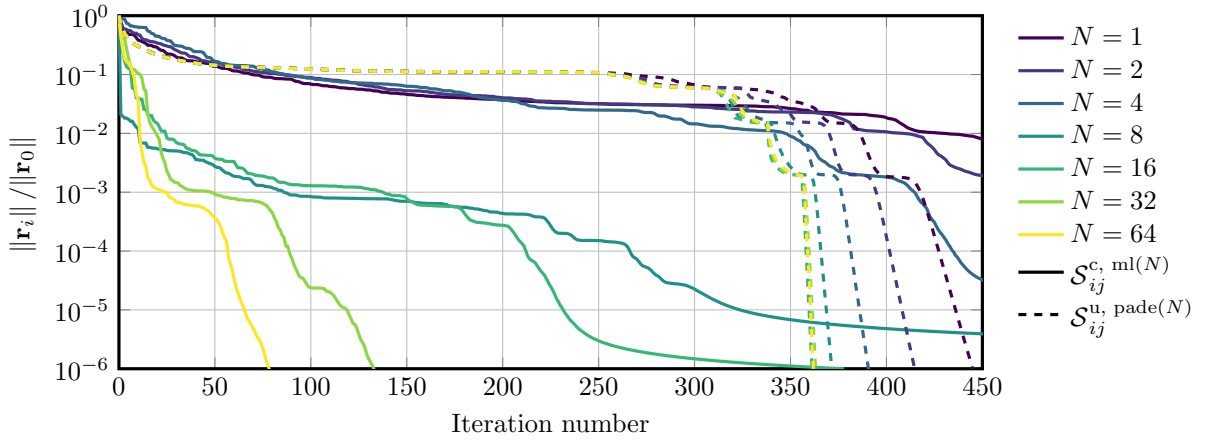


(b) Regularization with a mixed operator.

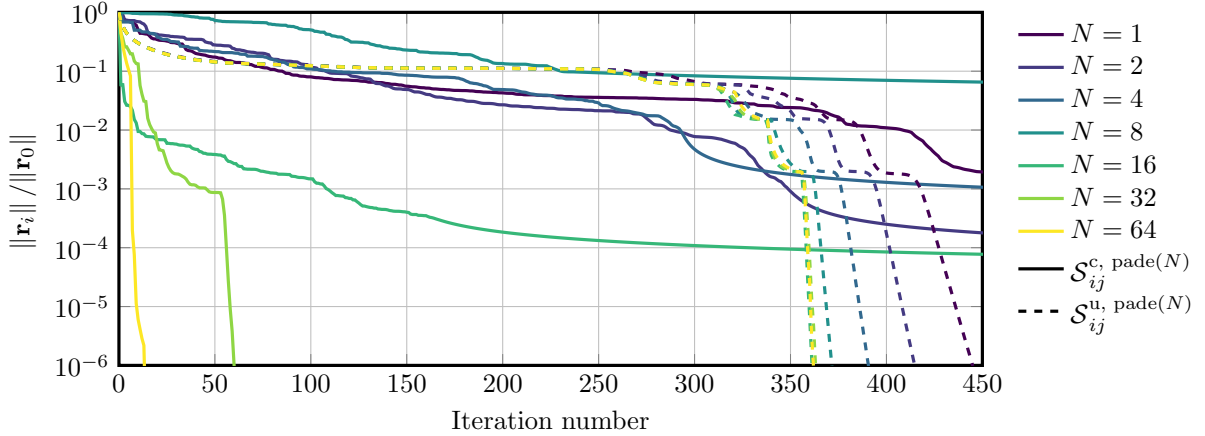
Figure 8: Regularized and mixed $PADE^c$ – rectangular cavity with $D = 8$ subdomains.

7.3. Impact of the number of auxiliary unknowns

Let us now investigate the impact of the number of auxiliary unknowns N appearing in $\mathcal{S}_{ij}^{u, \text{pade}(N)}$, $\mathcal{S}_{ij}^{c, \text{ml}(N)}$ and $\mathcal{S}_{ij}^{c, \text{pade}(N)}$ on the number of iteration of the GMRES solver. The numerical results are shown in Figure 9 for a numerical experiment involving $D = 8$ subdomains of equal size. It is clear from the data that the minimum value of N required for an acceptable convergence is $N_{\min}^{\text{data}} = 32$ for the ML^c and PADE^c operators, while it can be as low as $N_{\min}^{\text{data}} = 1$ for PADE^u . It is also evident that $\mathcal{S}_{ij}^{c, \text{pade}(N)}$ always performs better than $\mathcal{S}_{ij}^{c, \text{ml}(N)}$ when $N > N_{\min}^{\text{data}}$. On the other hand, while both $\mathcal{S}_{ij}^{c, \text{pade}(N)}$ and $\mathcal{S}_{ij}^{c, \text{ml}(N)}$ perform poorly when $N < N_{\min}^{\text{data}}$ compared with $\mathcal{S}_{ij}^{u, \text{pade}(N)}$, we can observe that $\mathcal{S}_{ij}^{c, \text{ml}(N)}$ behaves better than $\mathcal{S}_{ij}^{c, \text{pade}(N)}$. Last but not least, it is evident from Figure 9 that N has only a mild effect on the performance of $\mathcal{S}_{ij}^{u, \text{pade}(N)}$.



(a) Mittag-Leffler expansion.



(b) Padé expansion.

Figure 9: Convergence history of the GMRES solver for different number of auxiliary unknown in the case of $D = 8$ subdomains.

It is also interesting to compare the value of N_{\min}^{data} found experimentally and the value predicted with the pole criterion discussed in section 4.6. In this numerical experiment, the largest ℓ_{ij} is $\ell_{ij}^{\max} = \frac{7}{8}\ell$ and thus $N_{\min}^{\text{pole}} = 44$ according to the pole criterion (32). Consequently, N_{\min}^{pole} is a pessimistic estimation in this case, since $N_{\min}^{\text{data}} < N_{\min}^{\text{pole}}$.

7.4. Increase in the number of rectangular subdomains

In this section we focus on the impact of the number of subdomains D onto the GMRES iteration count, as shown in Figure 10 where scenarios involving more than 1000 iterations are not depicted. This implies that no data for $\mathcal{S}_{ij}^{c, oo0}$ are available. From this plot, it is clear that $\mathcal{S}_{ij}^{c, \text{pade}(64)}$ leads to an increase in the number of GMRES iterations with the optimal slope of $2D$, at least for the considered range of D . Let us mention also that the unbounded transmission operators exhibit a significantly larger slope, motivating thus the use of transmission conditions specifically devised for cavity problems. Furthermore let us note that $\mathcal{S}_{ij}^{u, \text{pade}(64)}$ and $\mathcal{S}_{ij}^{u, oo2}$ present the same slope, as they are both excellent localization of the unbounded DtN map. Concerning $\mathcal{S}_{ij}^{c, \text{ml}(64)}$, its performance remains good (but not as good as $\mathcal{S}_{ij}^{c, \text{pade}(64)}$) until $D = 12$ subdomains. Beyond this threshold, the required relative residual $\|\mathbf{r}_i\| / \|\mathbf{r}_0\|$ of 10^{-6} is suddenly out of reach. This phenomenon finds its root in the slow convergence of $\mathcal{S}_{ij}^{c, \text{ml}(N)}$ with respect to N , as increasing this value improves (yet mildly) this issue, as depicted in Figure 10 for $\mathcal{S}_{ij}^{c, \text{ml}(128)}$. Nonetheless, this $\mathcal{S}_{ij}^{c, \text{ml}(128)}$ operator still performs poorly as D increases.

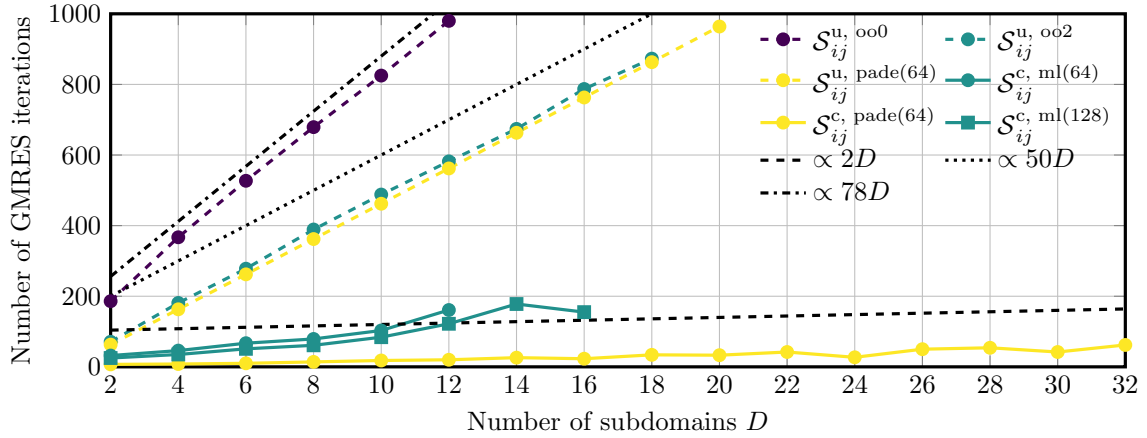


Figure 10: Number of GMRES iterations as a function of the number of subdomains.

7.5. Impact of the length-to-wavelength ratio

The dependence of the GMRES iteration count on the wavenumber is a major performance indicator of an OS scheme, and a numerical experiment analyzing this is therefore carried out. In this investigation the values of ℓ/λ_w are chosen close to an integer value, which corresponds to a cavity driven at a frequency close to one of its resonance frequencies. The computational domain is partitioned into $D = 8$ subdomains and the cavity is excited with double the amount of non-evanescent modes (this number depending on ℓ/λ_w). It is clear from the data shown in Figure 11 that the iteration count increases with ℓ/λ_w with the unbounded transmission operators. This behavior is however significantly improved with $\mathcal{S}_{ij}^{c, \text{ml}(N)}$ and the iteration count becomes almost independent from ℓ/λ_w with $\mathcal{S}_{ij}^{c, \text{pade}(N)}$, at least in the considered ℓ/λ_w range. Let us also note that similar results are obtained when ℓ/λ_w is selected away from a resonance.

7.6. Discussion

From the data gathered in the previous numerical examples, it is obvious that the $\mathcal{S}_{ij}^{c, oo0}$ operator is unreliable, as it leads to an extremely slow convergence. For this reason, this operator and its regularized variants are not further considered in this work.

It is also clear that for rectangular cavities the $\mathcal{S}_{ij}^{c, \text{pade}(N)}$ and $\mathcal{S}_{ij}^{c, \text{ml}(N)}$ operators converge with significantly less iterations than their unbounded alternatives, *i.e.* $\mathcal{S}_{ij}^{u, \text{pade}(N)}$, $\mathcal{S}_{ij}^{u, oo2}$ and $\mathcal{S}_{ij}^{u, oo0}$. Nonetheless, let us recall that the $\mathcal{S}_{ij}^{c, \text{ml}(N)}$ operator becomes unreliable when the number of subdomains D becomes too

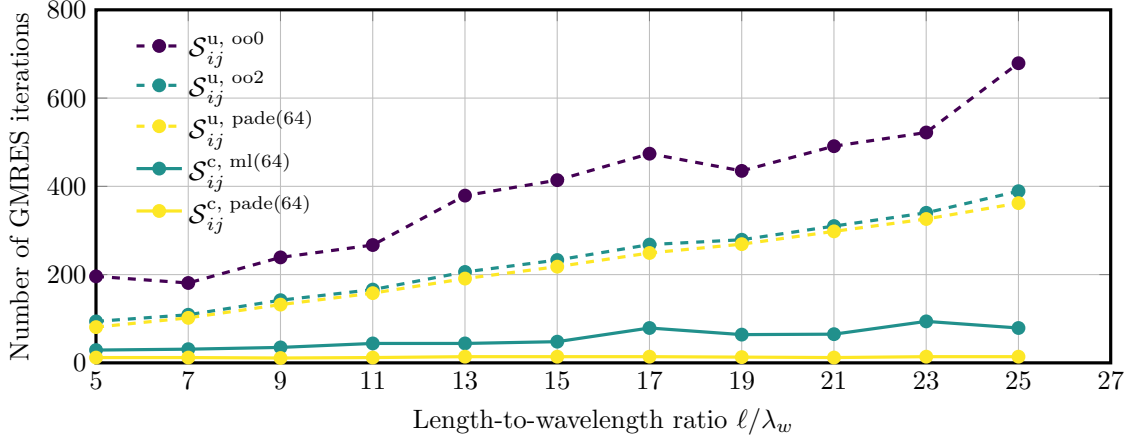


Figure 11: Number of GMRES iterations as a function of the length-to-wavelength ratio for a cavity with $D = 8$ subdomains.

large, which is however not the case for $\mathcal{S}_{ij}^{c, pade(N)}$. Furthermore, the novel operators are associated with an increased computational cost.

It is also worth noticing that the unbounded operator $\mathcal{S}_{ij}^{u, pade(N)}$ and $\mathcal{S}_{ij}^{u, oo2}$ lead to very similar convergence profiles, which is not surprising as they both are excellent approximations of the unbounded DtN map. For this reason, only the $\mathcal{S}_{ij}^{u, pade(N)}$ operator will be further considered.

Another interesting result concerns the impact of a change of the wavenumber on the convergence profile of the above transmission operators. For the considered range of length-to-wavelength ratios ℓ/λ_w , we observed that the $\mathcal{S}_{ij}^{c, pade(N)}$ behaves quasi-independently from ℓ/λ_w , while the other operators exhibit a (quasi) linear increase of the iteration count with ℓ/λ_w . Nonetheless, the slope of this increase remains small for $\mathcal{S}_{ij}^{c, ml(N)}$ when compared with $\mathcal{S}_{ij}^{u, oo0}$, $\mathcal{S}_{ij}^{u, oo2}$ and $\mathcal{S}_{ij}^{u, pade(N)}$.

Let us finally note that similar experiments were carried out on three-dimensional rectangular parallelepipedic cavities with a square cross-section of $h \times h$ and a length of ℓ . Results analogous to the above two-dimensional test cases were obtained.

8. Sensitivity to geometrical parameters

The previous section considered only one geometry (a rectangular cavity and its three-dimensional equivalent), which refers to the specific configuration used to devise the transmission operators discussed in section 4. Nonetheless, relevant simulations involve computational domains that differ from this original setting. We therefore discuss in this section two geometries deviating from the canonical one.

8.1. Trapezoidal geometry

For this first numerical experiment, let us consider an isosceles trapezoid whose base is characterized with a parameter δ , as the one depicted in Figure 12. This computational domain is partitioned into $D = 16$ subdomains and, as with the previous rectangular cavity, the aspect ratio ℓ/h equals 2 and the length-to-wavelength ratio ℓ/λ_w is approximately 25.001.

The number of GMRES iterations associated with various operators are shown in Figure 13 for different values of δ . It is clear from the depicted results that the $\mathcal{S}_{ij}^{c, pade(64)}$ operator quickly fails, as it does not reach the prescribed relative residual tolerance of $\|\mathbf{r}_i\|/\|\mathbf{r}_0\| = 10^{-6}$ already at $\delta = 4\%$, while the $\mathcal{S}_{ij}^{u, pade(64)}$ condition is rather stable with respect to the considered geometrical parameter. Regarding the $\mathcal{S}_{ij}^{c, ml(64)}$, while failing for $\delta = 4\%$ as with $\mathcal{S}_{ij}^{c, pade(64)}$, it provides again acceptable results up to $\delta = 16\%$ included. Let

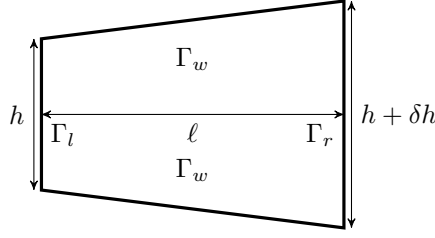


Figure 12: Isosceles trapezoid considered in the numerical experiment.

us also note that every time $\mathcal{S}_{ij}^{c, \text{pade}(64)}$ or $\mathcal{S}_{ij}^{c, \text{ml}(64)}$ converge, they do so with significantly less iterations than $\mathcal{S}_{ij}^{u, \text{pade}(64)}$.

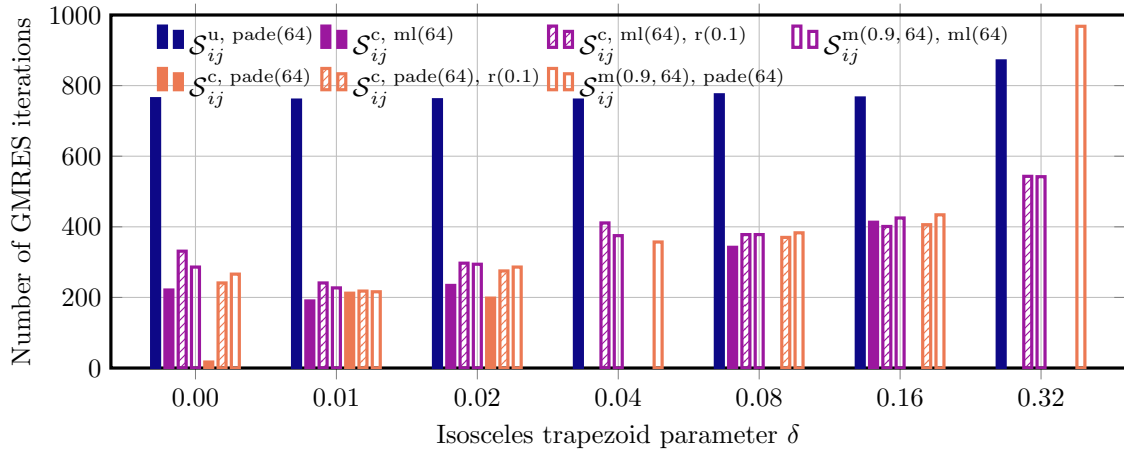


Figure 13: Iteration count of the GMRES solver when used on a trapezoidal geometry partitioned into $D = 16$ subdomains.

Figure 13 shows the behavior of the mixed operators as well (with $\varepsilon = 0.9$). It is worth mentioning that they always converge (yet without outperforming $\mathcal{S}_{ij}^{c, \text{pade}(64)}$ or $\mathcal{S}_{ij}^{c, \text{ml}(64)}$ when they converge) and require, most of the time, fewer iterations than the unbounded operator. In particular, $\mathcal{S}_{ij}^{m(0.9, 64), \text{pade}(64)}$ exhibits a quicker convergence than $\mathcal{S}_{ij}^{u, \text{pade}(64)}$ up to $\delta = 16\%$ included, while $\mathcal{S}_{ij}^{m(0.9, 64), \text{ml}(64)}$ converges systematically in less iterations than $\mathcal{S}_{ij}^{u, \text{pade}(64)}$.

Concerning the operators regularized with a constant imaginary part (with $\chi = 0.1$), we can directly observe that, when converging, they exhibit a behavior rather similar to the mixed one. Let us also mention that $\mathcal{S}_{ij}^{c, \text{ml}(64), r(0.1)}$ always converges in the studied range of the δ parameter.

8.2. Rectangular cavity involving obstacles – impact of the number of obstacles

Let us now study again a rectangular cavity, but let us introduce O circular obstacles in the domain. As in the previous case, we have $\ell/h = 2$ and $\ell/\lambda_w \approx 25.001$. Furthermore, we assume that the obstacles exhibit a hard-wall behavior and that each subdomain includes *at most* one obstacle located in its center. A sketch of a possible configuration is shown in Figure 14, with $O = 3$ obstacles and $D = 3$ subdomains.

We carry out a first numerical experiment consisting in determining the number of iterations as a function of the number of obstacles O . The obstacles are introduced by starting from the middle of the cavity and then by adding them equally on both sides. We consider a domain partitioning involving $D = 17$ subdomains, leading thus to a maximum number of obstacles of $O = 17$, and a radius of $R = 0.5\lambda_w$ for the obstacles. The results of this experiment are gathered in Figure 15. First of all, it is worth mentioning that when

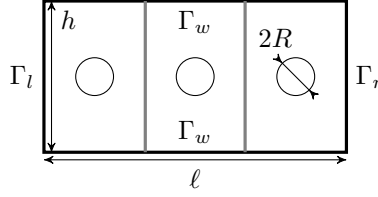


Figure 14: Rectangular cavity involving $O = 3$ obstacles and $D = 3$ subdomains.

$O = 1$, the transmission condition $\mathcal{S}_{ij}^{c, \text{pade}(64)}$ exhibits an excellent performance compared with the other operators. The operator $\mathcal{S}_{ij}^{c, \text{ml}(64)}$ also shows a good performance, in comparison with the unbounded Padé operator. This lead is however quickly taken over, as $\mathcal{S}_{ij}^{c, \text{pade}(64)}$ converges only for $O \leq 2$ obstacles⁹ and $\mathcal{S}_{ij}^{c, \text{ml}(64)}$ stops converging when $O \geq 11$.

Nonetheless, mixed operators keep on converging even with higher values of O , at least with $\varepsilon = 0.5$. Let us note that in this experiment, we used different values for the number of terms M and N in the mixed operators $\mathcal{S}_{ij}^{m(\varepsilon, M), \text{ml}(N)/\text{pade}(N)}$. Furthermore, while mixed operators tend to require less iterations than $\mathcal{S}_{ij}^{u, \text{pade}(64)}$ to converge, the difference tends to be rather modest.

This systematical convergence in the considered range of O is also exhibited by the Mittag-Leffler operator regularized with a constant imaginary term (with $\chi = 0.1$), which performs at least as well as its mixed counterpart, if not better. This is however not the case for $\mathcal{S}_{ij}^{c, \text{pade}(64), r(0.1)}$ that fails to converge for $O = 9$ obstacles.

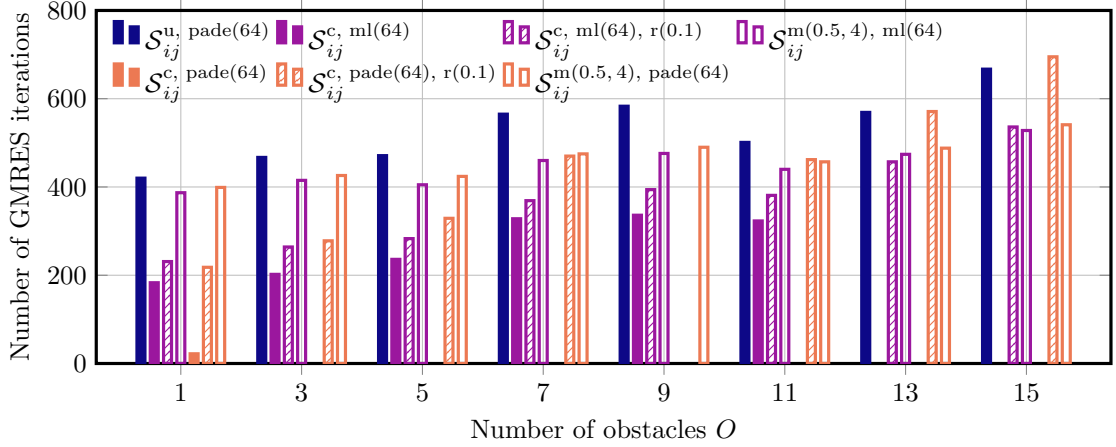


Figure 15: Iteration count of the GMRES solver when used on a rectangular cavity involving O obstacles of radius $R = 0.5\lambda_w$ and $D = 17$ subdomains.

8.3. Rectangular cavity involving obstacles – impact of the size of the obstacles

In the previous subsection we assumed a rather large radius for the obstacles compared with the wavelength and focused only on the number of obstacles. Let us now reverse the study and let us determine the impact of the obstacle size on the performance of the transmission operators. To this end, let us again consider a rectangular cavity with $D = 17$ subdomains and $O = 7$ obstacles of radius R and let us gather in Figure 16 the number of iterations required to solve this problem as R varies. It is clear from these data

⁹The case with $O = 2$ obstacles is not shown in Figure 15 for compactness reasons.

that the $\mathcal{S}_{ij}^{c, \text{pade}(N)}$ operator converges only for the three smallest values of R , while $\mathcal{S}_{ij}^{c, \text{ml}(N)}$ reaches the target tolerance in all the considered cases. Furthermore, both operators outperform $\mathcal{S}_{ij}^{u, \text{pade}(N)}$ in term of iteration count. As to the mixed operators (with $\varepsilon = 0.5$), they converge systematically, while not improving significantly the unbounded Padé transmission condition. Last but not least, operators regularized with a constant imaginary part (chosen here with $\chi = 0.1$) show a better behavior than their mixed counterpart.

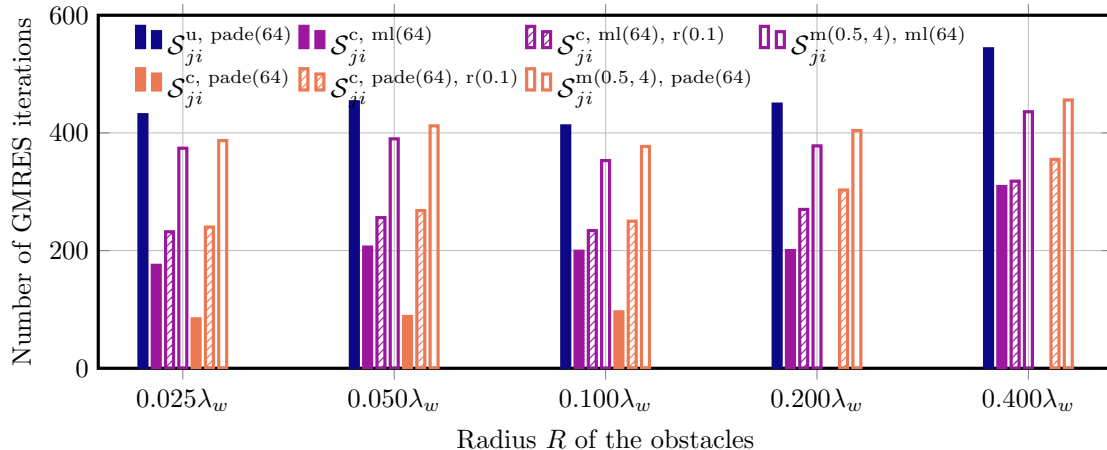


Figure 16: Iteration count of the GMRES solver when used on a rectangular cavity involving $O = 7$ obstacles and $D = 17$ subdomains.

8.4. Discussion

The above numerical experiments clearly show that the non-regularized operators $\mathcal{S}_{ij}^{c, \text{ml}(N)}$ and $\mathcal{S}_{ij}^{c, \text{pade}(N)}$ converge only when the computational domain does not deviate too much from the reference rectangular domain, the Mittag-Leffler operator being more robust in that aspect. Nevertheless, a regularization procedure (either with a constant imaginary part or with the unbounded version of the Padé-localized operator) alleviates this problem, up to an appropriate choice of the regularization parameter χ or ε . Those regularized operators do not however always perform better than unbounded ones, at least in the considered numerical examples.

9. Engineering test case: acoustic noise in a three-dimensional model of the helium vessel of a beamline cryostat

Going back to the experiment with a rectangular cavity filled with obstacles, it has been shown that the PADE^c operator shows a very fast convergence when the cavity *exhibits only one obstacle*, as shown in Figure 15. Additionally, the same behavior is observed for other configurations exhibiting a unique circular obstacle. A such characteristic can be very well suited when, for instance, simulating the acoustic noise in the helium vessel of a beamline cryostat, which basically consists of a rectangular cavity interrupted by a circular obstacle (*e.g.* see the cryostat discussed in [29]). Such acoustic noise analyses can become critical, for instance, when designing a cryogenic current comparator (CCC) with a large bore [30]. A CCC is one of the most sensitive instrument for measuring very low electric currents with high accuracy and can be used *e.g.* in particle accelerators for the non-destructive monitoring of slowly extracted charged particle beams (current intensities below $1\mu A$) [30].

Within this context, let us compare the behavior of the different transmission operators on a helium vessel model consisting in a rectangular parallelepipedic cavity interrupted with a cylindrical obstacle and partitioned into $D = 8$ subdomains. The model is excited with its first spatial mode, the length-to-wavelength ratio is chosen as $\ell/\lambda_w \simeq 12.5004$ and the cross-section is $h \times h$ with $h = \ell/2$. This numerical experiment

leads to the convergence history displayed in Figure 17 for each transmission operator. It is clear from these data that the $\mathcal{S}_{ij}^{c, \text{pade}(24)}$ leads to the quickest convergence and requires only 50 iterations to converge. Compared with the 93 iterations required by $\mathcal{S}_{ij}^{u, \text{pade}(24)}$, a reduction of the iteration count of approximately 46% is achieved. Figure 17 shows as well the impact of a light regularization of the PADE^c and ML^c operators. As expected, no performance gain is obtained, as the unregularized counterparts already converge well. For illustration purposes, the computed field map is available in Figure 18.

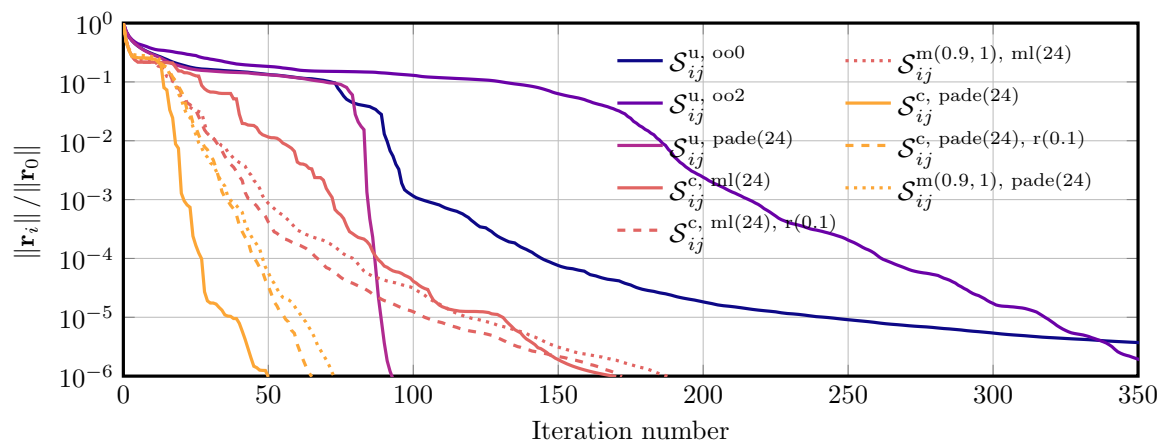


Figure 17: Convergence history of the GMRES solver – helium vessel of a beamline cryostat with $D = 8$ subdomains.

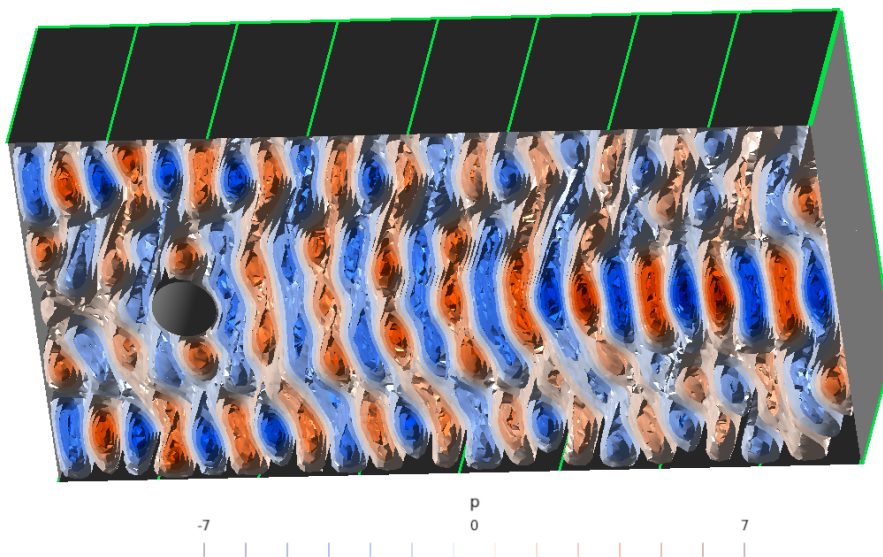


Figure 18: Field map of the simulated helium vessel (view rotated by 90° , subdomains are highlighted with green lines).

The above analysis would not be complete without considering the wall clock time¹⁰. As already discussed in section 7, the novel transmission operators optimized for cavity problems are associated with an increased computational cost, when compared with their unbounded counterparts. As a result, in the context of the considered acoustic study, the OO0^u and OO2^u operators lead to the fastest computations

¹⁰The simulations of section 9 were carried out on the NIC5 cluster hosted at the University of Liège, Belgium.

(*i.e.* approximately 3.5 and 3 hours respectively), despite their rather slow convergence. In comparison with OO2^u, the rational operators see their wall clock time increased by a factor of *i*) 2 for PADE^u, *ii*) 2.7 for ML^c and *iii*) 2.5 for PADE^c.

Before concluding this section, it is important to stress that the current implementation does not treat the auxiliary unknowns in the most efficient way. For instance, it assembles all auxiliary unknowns into a single large system. However, the extra unknowns stemming from the asymmetric nature of $\mathcal{S}_{ij}^{c, \text{ml}(N)/\text{pade}(N)}$ could be pulled out into smaller auxiliary systems, which could improve the overall computational time. Let us also mention that the OS iterative scheme can also be altered, such that all auxiliary unknowns are decoupled from the subproblems, as proposed in [31]. Such improvements are left for a future work.

10. Conclusion

In this work we presented new transmission operators for the Schwarz method optimized for time-harmonic Helmholtz problems in a rectangular cavity. Those operators rely on different localizations of the Dirichlet-to-Neumann map of this reference geometry. Three different strategies were considered for devising local approximations of the Fourier symbol of the DtN, namely: *i*) a zeroth-order Taylor approximation, *ii*) a truncated Mittag-Leffler partial fraction expansion and *iii*) a Padé approximant. Apart from the zeroth-order one, the proposed operators led to convergent iterative schemes when applied to the reference rectangular cavity. This convergence can however be quickly jeopardized when deviating from this reference case. Nevertheless, thanks to regularization procedures, a convergent optimized Schwarz method can be recovered.

The new operators optimized for cavity problems were also compared with operators optimized for unbounded geometries, yet applied to cavities. We showed with different test cases that those unbounded operators led to rather robust results with respect to geometries deviating from the reference rectangular one. Nevertheless, when considering small perturbations, the new operators exhibit a significant improvement in term of iteration count. The computational cost of the different transmission operators was also briefly discussed, as well as some possible improvements for reducing it.

Declaration of competing interest

The authors declare that they have no known competing financial interests or personal relationships that could have appeared to influence the work reported in this paper.

Acknowledgments

This research project has been funded by the Deutsche Forschungsgemeinschaft (DFG, German Research Foundation) – Project number 445906998. The work of Nicolas Marsic is also supported by the Graduate School CE within the Centre for Computational Engineering at the Technische Universität Darmstadt. Computational resources have been provided by the Consortium des Équipements de Calcul Intensif (CÉCI), funded by the Fonds de la Recherche Scientifique de Belgique (F.R.S.-FNRS) under Grant No. 2.5020.11 and by the Walloon Region. The authors would like to express their gratitude to Mr. Anthony Royer for his help with the GmshFEM and GmshDDM frameworks. In addition, the authors are grateful to Ms. Heike Koch, Mr. Achim Wagner, Mr. Dragos Munteanu, Mr. Christian Schmitt, Dr. Wolfgang Müller and Dr. David Colignon for the administrative and technical support.

Appendix A. Calculation of the convergence radius – non-overlapping case

In this appendix, let us briefly discuss the main steps of the calculation leading to the Fourier symbol of the Dirichlet-to-Neumann map shown in equation (9). To this end, we start with case $s^2 \neq k^2$, and write

the solutions of (6a) and (6d), together with the boundary conditions (6c) and (6f) and the definition (7). Formally, we obtain:

$$\left\{ \begin{array}{l} \widehat{p}_0^{n+1}(x, s) = P_0^{n+1}(s) \frac{\sinh \left[+\alpha \left(\frac{\ell}{2} + x \right) \right]}{\sinh \left[+\alpha \left(\frac{\ell}{2} + \gamma \right) \right]} \\ \widehat{p}_1^{n+1}(x, s) = P_1^{n+1}(s) \frac{\sinh \left[-\alpha \left(\frac{\ell}{2} - x \right) \right]}{\sinh \left[-\alpha \left(\frac{\ell}{2} - \gamma \right) \right]} \end{array} \right. \quad \forall x \in \left[-\frac{\ell}{2}, \gamma \right], \forall s \in \mathbb{S}, s^2 \neq k^2, \quad (\text{A.1a})$$

$$\forall x \in \left[\gamma, +\frac{\ell}{2} \right], \forall s \in \mathbb{S}, s^2 \neq k^2, \quad (\text{A.1b})$$

where

$$\alpha(s) = \begin{cases} -j\sqrt{k^2 - s^2} & \text{if } s^2 < k^2, \\ 0 & \text{if } s^2 = k^2, \\ \sqrt{s^2 - k^2} & \text{if } s^2 > k^2. \end{cases} \quad (\text{A.2a})$$

$$\text{if } s^2 = k^2, \quad (\text{A.2b})$$

$$\text{if } s^2 > k^2. \quad (\text{A.2c})$$

This solution can then be derived with respect to x and the result evaluated at the interface between the subdomains, *i.e.* at $x = \gamma(t) = t\ell - \ell/2$ with $t \in [0, 1]$ as discussed in section 2. We thus have that

$$\left\{ \begin{array}{l} \left. \frac{\partial \widehat{p}_0^{n+1}}{\partial x}(x, s) \right|_{x=\gamma(t)} = \alpha P_0^{n+1} \coth[+\alpha t\ell] \\ \left. \frac{\partial \widehat{p}_1^{n+1}}{\partial x}(x, s) \right|_{x=\gamma(t)} = \alpha P_1^{n+1} \coth[-\alpha(1-t)\ell] \end{array} \right. \quad \forall s \in \mathbb{S}, s^2 \neq k^2, \quad (\text{A.3a})$$

$$\forall s \in \mathbb{S}, s^2 \neq k^2. \quad (\text{A.3b})$$

The convergence radius $\rho(s)$ is then obtained by simplifying the transmission conditions (6b) and (6e) with the above expressions. In particular, we can write

$$\left\{ \begin{array}{l} P_0^{n+1} = P_0^{n-1} \frac{\lambda_{10} - \alpha \coth[\alpha t\ell]}{\lambda_{10} + \alpha \coth[\alpha(1-t)\ell]} \frac{\lambda_{01} - \alpha \coth[\alpha(1-t)\ell]}{\lambda_{01} + \alpha \coth[\alpha t\ell]} = P_0^{n-1} \rho^2(s), \\ P_1^{n+1} = P_1^{n-1} \frac{\lambda_{01} - \alpha \coth[\alpha(1-t)\ell]}{\lambda_{01} + \alpha \coth[\alpha t\ell]} \frac{\lambda_{10} - \alpha \coth[\alpha t\ell]}{\lambda_{10} + \alpha \coth[\alpha(1-t)\ell]} = P_1^{n-1} \rho^2(s). \end{array} \right. \quad (\text{A.4a})$$

$$\left. \right. \quad (\text{A.4b})$$

Equation (9) is thus recovered, for the case $s^2 \neq k^2$, by identifying the above terms and by exploiting the definition of $\alpha(s)$, ℓ_{01} and ℓ_{10} , that is

$$\left\{ \begin{array}{l} \ell_{01} = t\ell, \\ \ell_{10} = (1-t)\ell. \end{array} \right. \quad (\text{A.5a})$$

$$\left. \right. \quad (\text{A.5b})$$

Let us now treat the case $s^2 = k^2$. In this case $\widehat{p}_i^{n+1}(x, s)$ writes

$$\left\{ \begin{array}{l} \widehat{p}_0^{n+1}(x, s) = P_0^{n+1} \frac{x + \ell/2}{\gamma + \ell/2} \\ \widehat{p}_1^{n+1}(x, s) = P_1^{n+1} \frac{x - \ell/2}{\gamma - \ell/2} \end{array} \right. \quad \forall x \in \left[-\frac{\ell}{2}, \gamma \right], s^2 = k^2, \quad (\text{A.6a})$$

$$\forall x \in \left[\gamma, +\frac{\ell}{2} \right], s^2 = k^2, \quad (\text{A.6b})$$

and its derivative evaluated at $x = \gamma$ is simply:

$$\left\{ \begin{array}{l} \frac{\partial \widehat{p}_0^{n+1}}{\partial x}(x, s) \Big|_{x=\gamma(t)} = +P_0^{n+1} \frac{1}{t\ell} \\ \frac{\partial \widehat{p}_1^{n+1}}{\partial x}(x, s) \Big|_{x=\gamma(t)} = -P_1^{n+1} \frac{1}{(1-t)\ell} \end{array} \right. \quad \forall s \in \mathbb{S}, s^2 = k^2, \quad (\text{A.7a})$$

$$\left\{ \begin{array}{l} \frac{\partial \widehat{p}_0^{n+1}}{\partial x}(x, s) \Big|_{x=\gamma(t)} = +P_0^{n+1} \frac{1}{t\ell} \\ \frac{\partial \widehat{p}_1^{n+1}}{\partial x}(x, s) \Big|_{x=\gamma(t)} = -P_1^{n+1} \frac{1}{(1-t)\ell} \end{array} \right. \quad \forall s \in \mathbb{S}, s^2 = k^2. \quad (\text{A.7b})$$

Therefore, the transmission conditions (6b) and (6e) become

$$\left\{ \begin{array}{l} P_0^{n+1} = P_0^{n-1} \frac{\lambda_{10} - \frac{1}{t\ell}}{\lambda_{10} + \frac{1}{(1-t)\ell}} \frac{\lambda_{01} - \frac{1}{(1-t)\ell}}{\lambda_{01} + \frac{1}{t\ell}} = P_0^{n-1} \rho^2(s = k), \\ P_1^{n+1} = P_1^{n-1} \frac{\lambda_{01} - \frac{1}{(1-t)\ell}}{\lambda_{01} + \frac{1}{t\ell}} \frac{\lambda_{10} - \frac{1}{t\ell}}{\lambda_{10} + \frac{1}{(1-t)\ell}} = P_1^{n-1} \rho^2(s = k), \end{array} \right. \quad (\text{A.8a})$$

$$\left\{ \begin{array}{l} P_0^{n+1} = P_0^{n-1} \frac{\lambda_{10} - \frac{1}{t\ell}}{\lambda_{10} + \frac{1}{(1-t)\ell}} \frac{\lambda_{01} - \frac{1}{(1-t)\ell}}{\lambda_{01} + \frac{1}{t\ell}} = P_0^{n-1} \rho^2(s = k), \\ P_1^{n+1} = P_1^{n-1} \frac{\lambda_{01} - \frac{1}{(1-t)\ell}}{\lambda_{01} + \frac{1}{t\ell}} \frac{\lambda_{10} - \frac{1}{t\ell}}{\lambda_{10} + \frac{1}{(1-t)\ell}} = P_1^{n-1} \rho^2(s = k), \end{array} \right. \quad (\text{A.8b})$$

revealing thus the convergence radius $\rho(s = k)$. Again, equation (9) is recovered, for the case $s^2 = k^2$, by identifying the above terms and by exploiting the definition of ℓ_{01} and ℓ_{10} .

Appendix B. Calculation of the convergence radius – overlapping case

Let us now assume an overlap of 2δ such that Σ_{01} is located at $\gamma_0 = \gamma + \delta$ and Σ_{10} is located at $\gamma_1 = \gamma - \delta$, where $\gamma(t) = t\ell - \ell/2$ with $t \in [0, 1]$ as in the previous appendix. In the case $s^2 \neq k^2$, the overlapping variant of (6a) and (6d), together with the boundary conditions (6c) and (6f) and the definition (7) admits the following solutions:

$$\left\{ \begin{array}{l} \widehat{p}_0^{n+1}(x, s) = P_0^{n+1}(s) \frac{\sinh \left[+\alpha \left(\frac{\ell}{2} + x \right) \right]}{\sinh \left[+\alpha \left(\frac{\ell}{2} + \gamma_0 \right) \right]} \\ \widehat{p}_1^{n+1}(x, s) = P_1^{n+1}(s) \frac{\sinh \left[-\alpha \left(\frac{\ell}{2} - x \right) \right]}{\sinh \left[-\alpha \left(\frac{\ell}{2} - \gamma_1 \right) \right]} \end{array} \right. \quad \forall x \in \left[-\frac{\ell}{2}, \gamma_0 \right], \forall s \in \mathbb{S}, s^2 \neq k^2, \quad (\text{B.1a})$$

$$\left\{ \begin{array}{l} \widehat{p}_0^{n+1}(x, s) = P_0^{n+1}(s) \frac{\sinh \left[+\alpha \left(\frac{\ell}{2} + x \right) \right]}{\sinh \left[+\alpha \left(\frac{\ell}{2} + \gamma_0 \right) \right]} \\ \widehat{p}_1^{n+1}(x, s) = P_1^{n+1}(s) \frac{\sinh \left[-\alpha \left(\frac{\ell}{2} - x \right) \right]}{\sinh \left[-\alpha \left(\frac{\ell}{2} - \gamma_1 \right) \right]} \end{array} \right. \quad \forall x \in \left[\gamma_1, \frac{\ell}{2} \right], \forall s \in \mathbb{S}, s^2 \neq k^2, \quad (\text{B.1b})$$

which is similar as for the non-overlapping case but with interfaces located at different positions, $x = \gamma_0$ and $x = \gamma_1$, instead of a unique one, $x = \gamma$. After evaluating those two solutions at $x = \gamma_0$ and $x = \gamma_1$, we obtain:

$$\left\{ \begin{array}{l} \widehat{p}_0^{n+1}(\gamma_0, s) = P_0^{n+1}(s) \\ \widehat{p}_1^{n+1}(\gamma_0, s) = P_1^{n+1}(s) \frac{\sinh \left[\alpha \left(\frac{\ell}{2} - \gamma - \delta \right) \right]}{\sinh \left[\alpha \left(\frac{\ell}{2} - \gamma + \delta \right) \right]} \end{array} \right. \quad \forall s \in \mathbb{S}, s^2 \neq k^2, \quad (\text{B.2a})$$

$$\left\{ \begin{array}{l} \widehat{p}_0^{n+1}(\gamma_0, s) = P_0^{n+1}(s) \\ \widehat{p}_1^{n+1}(\gamma_0, s) = P_1^{n+1}(s) \frac{\sinh \left[\alpha \left(\frac{\ell}{2} - \gamma - \delta \right) \right]}{\sinh \left[\alpha \left(\frac{\ell}{2} - \gamma + \delta \right) \right]} \end{array} \right. \quad \forall s \in \mathbb{S}, s^2 \neq k^2, \quad (\text{B.2b})$$

and

$$\left\{ \begin{array}{l} \widehat{p}_0^{n+1}(\gamma_1, s) = P_0^{n+1}(s) \frac{\sinh \left[\alpha \left(\frac{\ell}{2} + \gamma - \delta \right) \right]}{\sinh \left[\alpha \left(\frac{\ell}{2} + \gamma + \delta \right) \right]} \\ \widehat{p}_1^{n+1}(\gamma_1, s) = P_1^{n+1}(s) \end{array} \right. \quad \forall s \in \mathbb{S}, s^2 \neq k^2, \quad (\text{B.3a})$$

$$\left\{ \begin{array}{l} \widehat{p}_0^{n+1}(\gamma_1, s) = P_0^{n+1}(s) \frac{\sinh \left[\alpha \left(\frac{\ell}{2} + \gamma - \delta \right) \right]}{\sinh \left[\alpha \left(\frac{\ell}{2} + \gamma + \delta \right) \right]} \\ \widehat{p}_1^{n+1}(\gamma_1, s) = P_1^{n+1}(s) \end{array} \right. \quad \forall s \in \mathbb{S}, s^2 \neq k^2. \quad (\text{B.3b})$$

Regarding the derivatives with respect to x of $\widehat{p}_0^{n+1}(x, s)$ and $\widehat{p}_0^{n+1}(x, s)$ at $x = \gamma_0$ and $x = \gamma_1$, we have:

$$\left\{ \begin{array}{l} \left. \frac{\partial \widehat{p}_0^{n+1}}{\partial x}(x, s) \right|_{x=\gamma_0} = +\alpha P_0^{n+1} \frac{\cosh \left[\alpha \left(\frac{\ell}{2} + \gamma + \delta \right) \right]}{\sinh \left[\alpha \left(\frac{\ell}{2} + \gamma + \delta \right) \right]} \\ \left. \frac{\partial \widehat{p}_1^{n+1}}{\partial x}(x, s) \right|_{x=\gamma_0} = -\alpha P_1^{n+1} \frac{\cosh \left[\alpha \left(\frac{\ell}{2} - \gamma - \delta \right) \right]}{\sinh \left[\alpha \left(\frac{\ell}{2} - \gamma + \delta \right) \right]} \end{array} \right. \quad \forall s \in \mathbb{S}, s^2 \neq k^2, \quad (\text{B.4a})$$

$$\left\{ \begin{array}{l} \left. \frac{\partial \widehat{p}_0^{n+1}}{\partial x}(x, s) \right|_{x=\gamma_1} = +\alpha P_0^{n+1} \frac{\cosh \left[\alpha \left(\frac{\ell}{2} + \gamma - \delta \right) \right]}{\sinh \left[\alpha \left(\frac{\ell}{2} + \gamma + \delta \right) \right]} \\ \left. \frac{\partial \widehat{p}_1^{n+1}}{\partial x}(x, s) \right|_{x=\gamma_1} = -\alpha P_1^{n+1} \frac{\cosh \left[\alpha \left(\frac{\ell}{2} - \gamma + \delta \right) \right]}{\sinh \left[\alpha \left(\frac{\ell}{2} - \gamma + \delta \right) \right]} \end{array} \right. \quad \forall s \in \mathbb{S}, s^2 \neq k^2. \quad (\text{B.5b})$$

and

$$\left\{ \begin{array}{l} \left. \frac{\partial \widehat{p}_0^{n+1}}{\partial x}(x, s) \right|_{x=\gamma_1} = +\alpha P_0^{n+1} \frac{\cosh \left[\alpha \left(\frac{\ell}{2} + \gamma - \delta \right) \right]}{\sinh \left[\alpha \left(\frac{\ell}{2} + \gamma + \delta \right) \right]} \\ \left. \frac{\partial \widehat{p}_1^{n+1}}{\partial x}(x, s) \right|_{x=\gamma_1} = -\alpha P_1^{n+1} \frac{\cosh \left[\alpha \left(\frac{\ell}{2} - \gamma + \delta \right) \right]}{\sinh \left[\alpha \left(\frac{\ell}{2} - \gamma + \delta \right) \right]} \end{array} \right. \quad \forall s \in \mathbb{S}, s^2 \neq k^2. \quad (\text{B.5a})$$

Therefore, the overlapping variant of the transmission conditions (6b) and (6e) leads to

$$\left\{ \begin{array}{l} P_0^{n+1} = P_0^{n-1} \frac{\lambda_{10} - \alpha \coth \left[\alpha \left(\frac{\ell}{2} + \gamma - \delta \right) \right]}{\lambda_{10} + \alpha \coth \left[\alpha \left(\frac{\ell}{2} - \gamma + \delta \right) \right]} \frac{\lambda_{01} - \alpha \coth \left[\alpha \left(\frac{\ell}{2} - \gamma - \delta \right) \right]}{\lambda_{01} + \alpha \coth \left[\alpha \left(\frac{\ell}{2} + \gamma + \delta \right) \right]} \\ \frac{\sinh \left[\alpha \left(\frac{\ell}{2} + \gamma - \delta \right) \right]}{\sinh \left[\alpha \left(\frac{\ell}{2} + \gamma + \delta \right) \right]} \frac{\sinh \left[\alpha \left(\frac{\ell}{2} - \gamma - \delta \right) \right]}{\sinh \left[\alpha \left(\frac{\ell}{2} - \gamma + \delta \right) \right]} = P_0^{n-1} \rho^2, \\ P_1^{n+1} = P_1^{n-1} \frac{\lambda_{01} - \alpha \coth \left[\alpha \left(\frac{\ell}{2} - \gamma - \delta \right) \right]}{\lambda_{01} + \alpha \coth \left[\alpha \left(\frac{\ell}{2} + \gamma + \delta \right) \right]} \frac{\lambda_{10} - \alpha \coth \left[\alpha \left(\frac{\ell}{2} + \gamma - \delta \right) \right]}{\lambda_{10} + \alpha \coth \left[\alpha \left(\frac{\ell}{2} - \gamma + \delta \right) \right]} \\ \frac{\sinh \left[\alpha \left(\frac{\ell}{2} - \gamma - \delta \right) \right]}{\sinh \left[\alpha \left(\frac{\ell}{2} - \gamma + \delta \right) \right]} \frac{\sinh \left[\alpha \left(\frac{\ell}{2} + \gamma - \delta \right) \right]}{\sinh \left[\alpha \left(\frac{\ell}{2} + \gamma + \delta \right) \right]} = P_1^{n-1} \rho^2. \end{array} \right. \quad (\text{B.6a})$$

$$\left\{ \begin{array}{l} P_0^{n+1} = P_0^{n-1} \frac{\lambda_{10} - \alpha \coth \left[\alpha \left(\frac{\ell}{2} + \gamma - \delta \right) \right]}{\lambda_{10} + \alpha \coth \left[\alpha \left(\frac{\ell}{2} - \gamma + \delta \right) \right]} \frac{\lambda_{01} - \alpha \coth \left[\alpha \left(\frac{\ell}{2} - \gamma - \delta \right) \right]}{\lambda_{01} + \alpha \coth \left[\alpha \left(\frac{\ell}{2} + \gamma + \delta \right) \right]} \\ \frac{\sinh \left[\alpha \left(\frac{\ell}{2} + \gamma - \delta \right) \right]}{\sinh \left[\alpha \left(\frac{\ell}{2} + \gamma + \delta \right) \right]} \frac{\sinh \left[\alpha \left(\frac{\ell}{2} - \gamma - \delta \right) \right]}{\sinh \left[\alpha \left(\frac{\ell}{2} - \gamma + \delta \right) \right]} = P_0^{n-1} \rho^2, \\ P_1^{n+1} = P_1^{n-1} \frac{\lambda_{01} - \alpha \coth \left[\alpha \left(\frac{\ell}{2} - \gamma - \delta \right) \right]}{\lambda_{01} + \alpha \coth \left[\alpha \left(\frac{\ell}{2} + \gamma + \delta \right) \right]} \frac{\lambda_{10} - \alpha \coth \left[\alpha \left(\frac{\ell}{2} + \gamma - \delta \right) \right]}{\lambda_{10} + \alpha \coth \left[\alpha \left(\frac{\ell}{2} - \gamma + \delta \right) \right]} \\ \frac{\sinh \left[\alpha \left(\frac{\ell}{2} - \gamma - \delta \right) \right]}{\sinh \left[\alpha \left(\frac{\ell}{2} - \gamma + \delta \right) \right]} \frac{\sinh \left[\alpha \left(\frac{\ell}{2} + \gamma - \delta \right) \right]}{\sinh \left[\alpha \left(\frac{\ell}{2} + \gamma + \delta \right) \right]} = P_1^{n-1} \rho^2. \end{array} \right. \quad (\text{B.6b})$$

Equation (11) is thus recovered, for the case $s^2 \neq k^2$, by identifying the above terms and by exploiting the definitions of $\alpha(s)$, ℓ_{01} , ℓ_{10} , ℓ'_{01} and ℓ'_{10} , that are:

$$\left\{ \begin{array}{l} \ell_{01} = \frac{\ell}{2} + \gamma + \delta, \\ \ell_{10} = \frac{\ell}{2} - \gamma + \delta, \\ \ell'_{01} = \frac{\ell}{2} + \gamma - \delta, \\ \ell'_{10} = \frac{\ell}{2} - \gamma - \delta. \end{array} \right. \quad (\text{B.7a})$$

$$\left\{ \begin{array}{l} \ell_{01} = \frac{\ell}{2} + \gamma + \delta, \\ \ell_{10} = \frac{\ell}{2} - \gamma + \delta, \end{array} \right. \quad (\text{B.7b})$$

$$\left\{ \begin{array}{l} \ell'_{01} = \frac{\ell}{2} + \gamma - \delta, \\ \ell'_{10} = \frac{\ell}{2} - \gamma - \delta, \end{array} \right. \quad (\text{B.7c})$$

$$\left\{ \begin{array}{l} \ell'_{01} = \frac{\ell}{2} + \gamma - \delta, \\ \ell'_{10} = \frac{\ell}{2} - \gamma - \delta. \end{array} \right. \quad (\text{B.7d})$$

Finally, the case $s^2 = k^2$ is obtained in a similar way, which leads to following recursion

$$\left\{ \begin{array}{l} P_0^{n+1} = P_0^{n-1} \frac{\lambda_{10} - \left(\frac{\ell}{2} + \gamma - \delta\right)^{-1} \lambda_{01} - \left(\frac{\ell}{2} - \gamma - \delta\right)^{-1} \frac{\frac{\ell}{2} + \gamma - \delta}{\frac{\ell}{2} - \gamma - \delta}}{\lambda_{10} + \left(\frac{\ell}{2} - \gamma + \delta\right)^{-1} \lambda_{01} + \left(\frac{\ell}{2} + \gamma + \delta\right)^{-1} \frac{\frac{\ell}{2} + \gamma + \delta}{\frac{\ell}{2} - \gamma + \delta}} = P_0^{n-1} \rho^2, \\ P_1^{n+1} = P_1^{n-1} \frac{\lambda_{01} - \left(\frac{\ell}{2} - \gamma - \delta\right)^{-1} \lambda_{10} - \left(\frac{\ell}{2} + \gamma - \delta\right)^{-1} \frac{\ell_2 - \gamma - \delta}{\ell_2 + \gamma - \delta}}{\lambda_{01} + \left(\frac{\ell}{2} + \gamma + \delta\right)^{-1} \lambda_{10} + \left(\frac{\ell}{2} - \gamma + \delta\right)^{-1} \frac{\ell_2 - \gamma + \delta}{\ell_2 + \gamma + \delta}} = P_1^{n-1} \rho^2, \end{array} \right. \quad (\text{B.8a})$$

$$\left\{ \begin{array}{l} P_0^{n+1} = P_0^{n-1} \frac{\lambda_{10} - \left(\frac{\ell}{2} + \gamma - \delta\right)^{-1} \lambda_{01} - \left(\frac{\ell}{2} - \gamma - \delta\right)^{-1} \frac{\frac{\ell}{2} + \gamma - \delta}{\frac{\ell}{2} - \gamma - \delta}}{\lambda_{10} + \left(\frac{\ell}{2} - \gamma + \delta\right)^{-1} \lambda_{01} + \left(\frac{\ell}{2} + \gamma + \delta\right)^{-1} \frac{\frac{\ell}{2} + \gamma + \delta}{\frac{\ell}{2} - \gamma + \delta}} = P_0^{n-1} \rho^2, \\ P_1^{n+1} = P_1^{n-1} \frac{\lambda_{01} - \left(\frac{\ell}{2} - \gamma - \delta\right)^{-1} \lambda_{10} - \left(\frac{\ell}{2} + \gamma - \delta\right)^{-1} \frac{\ell_2 - \gamma - \delta}{\ell_2 + \gamma - \delta}}{\lambda_{01} + \left(\frac{\ell}{2} + \gamma + \delta\right)^{-1} \lambda_{10} + \left(\frac{\ell}{2} - \gamma + \delta\right)^{-1} \frac{\ell_2 - \gamma + \delta}{\ell_2 + \gamma + \delta}} = P_1^{n-1} \rho^2, \end{array} \right. \quad (\text{B.8b})$$

revealing thus the convergence radius. Equation (11) is again recovered, for the case $s^2 = k^2$, by identifying the above terms and by exploiting the definitions of $\alpha(s)$, ℓ_{01} , ℓ_{10} , ℓ'_{01} and ℓ'_{10} .

References

- [1] F. Ihlenburg, I. Babuška, Finite element solution of the Helmholtz equation with high wave number part I: The h-version of the FEM, *Computers & Mathematics with Applications* 30 (9) (1995) 9–37. doi:10.1016/0898-1221(95)00144-N.
- [2] O. G. Ernst, M. J. Gander, Why it is difficult to solve Helmholtz problems with classical iterative methods, in: I. G. Graham, T. Y. Hou, O. Lakkis, R. Scheichl (Eds.), *Numerical Analysis of Multiscale Problems*, Vol. 83 of *Lecture Notes in Computational Science and Engineering*, 2012, pp. 325–363. doi:10.1007/978-3-642-22061-6_10.
- [3] F. Ihlenburg, I. Babuška, Finite element solution of the Helmholtz equation with high wave number part II: The h-version of the FEM, *SIAM Journal on Numerical Analysis* 34 (1) (1997) 315–358. doi:10.1137/S0036142994272337.
- [4] A. Moiola, E. A. Spence, Is the Helmholtz equation really sign-indefinite?, *SIAM Review* 56 (2) (2014) 274–312. doi:10.1137/120901301.
- [5] G. C. Diwan, A. Moiola, E. A. Spence, Can coercive formulations lead to fast and accurate solution of the Helmholtz equation?, *Journal of Computational and Applied Mathematics* 352 (2019) 110–131. doi:10.1016/j.cam.2018.11.035.
- [6] M. Yannakakis, Computing the minimum fill-in is NP-complete, *SIAM Journal on Algebraic Discrete Methods* 2 (1) (1981) 77–79. doi:10.1137/0602010.
- [7] N. Marsic, H. De Gersem, G. Demésy, A. Nicolet, C. Geuzaine, Modal analysis of the ultrahigh finesse Haroche QED cavity, *New Journal of Physics* 20 (4) (2018) 043058. doi:10.1088/1367-2630/aab6fd.
- [8] B. Després, Décomposition de domaine et problème de Helmholtz, *Comptes Rendus de l'Académie des Sciences* 311 (1990) 313–316.
URL <https://gallica.bnf.fr/ark:/12148/bpt6k57815213>
- [9] Y. Boubendir, An analysis of the BEM-FEM non-overlapping domain decomposition method for a scattering problem, *Journal of Computational and Applied Mathematics* 204 (2) (2007) 282–291. doi:10.1016/j.cam.2006.02.044.
- [10] M. J. Gander, F. Magoulès, F. Nataf, Optimized Schwarz methods without overlap for the Helmholtz equation, *SIAM Journal on Scientific Computing* 24 (1) (2002) 38–60. doi:10.1137/S1064827501387012.
- [11] Y. Boubendir, X. Antoine, C. Geuzaine, A quasi-optimal non-overlapping domain decomposition algorithm for the Helmholtz equation, *Journal of Computational Physics* 231 (2) (2012) 262–280. doi:10.1016/j.jcp.2011.08.007.
- [12] A. Vion, C. Geuzaine, Double sweep preconditioner for optimized Schwarz methods applied to the Helmholtz problem, *Journal of Computational Physics* 266 (2014) 171–190. doi:10.1016/j.jcp.2014.02.015.
- [13] M. J. Gander, H. Zhang, A class of iterative solvers for the Helmholtz equation: Factorizations, sweeping preconditioners, source transfer, single layer potentials, polarized traces, and optimized Schwarz methods, *SIAM Review* 61 (1) (2019) 3–76. doi:10.1137/16m109781x.
- [14] V. Dolean, P. Jolivet, F. Nataf, *An introduction to domain decomposition methods: algorithms, theory and parallel implementation*, *Society for Industrial and Applied Mathematics*, 2015. doi:10.1137/1.9781611974065.
- [15] Z. Peng, J.-F. Lee, Non-conformal domain decomposition method with mixed true second order transmission condition for solving large finite antenna arrays, *IEEE Transactions on Antennas and Propagation* 59 (5) (2011) 1638–1651. doi:10.1109/TAP.2011.2123067.
- [16] P.-H. Tournier, M. Bonazzoli, V. Dolean, F. Rapetti, F. Hecht, F. Nataf, I. Aliferis, I. El Kanfoud, C. Migliaccio, M. de Buhan, M. Darbas, S. Semenov, C. Pichot, Numerical modeling and high-speed parallel computing: New perspectives on tomographic microwave imaging for brain stroke detection and monitoring., *IEEE Antennas and Propagation Magazine* 59 (5) (2017) 98–110. doi:10.1109/map.2017.2731199.
- [17] N. Marsic, C. Waltz, J.-F. Lee, C. Geuzaine, Domain decomposition methods for time-harmonic electromagnetic waves with high order whitney forms, *IEEE Transactions on Magnetics* 52 (3) (2016) 1–4. doi:10.1109/TMAG.2015.2476510.
- [18] B. E. A. Saleh, M. C. Teich, *Fundamentals of Photonics*, 2nd Edition, Wiley-Interscience, 2007. doi:10.1002/0471213748.
- [19] K. Ko, N. Folwell, L. Ge, A. Guetz, L. Lee, Z. Li, C. Ng, E. Prudencio, G. Schussman, R. Uplenchwar, L. Xiao, Advances in electromagnetic modelling through high performance computing, *Physica C: Superconductivity and its Applications* 441 (1-2) (2006) 258–262. doi:10.1016/j.physc.2006.03.139.
- [20] L. V. Ahlfors, *Complex analysis*, 3rd Edition, McGraw-Hill, New York, NY, 1979.
- [21] G. A. Baker, P. Graves-Morris, *Padé Approximants*, 2nd Edition, Cambridge University Press, 1996. doi:10.1017/cbo9780511530074.

- [22] K. Oldham, J. Myland, J. Spanier, *An Atlas of Functions*, 2nd Edition, Springer-Verlag New York, 2009. doi:10.1007/978-0-387-48807-3.
- [23] D. A. Bini, L. Robol, Solving secular and polynomial equations: A multiprecision algorithm, *Journal of Computational and Applied Mathematics* 272 (2014) 276–292. doi:10.1016/j.cam.2013.04.037.
- [24] F. A. Milinazzo, C. A. Zala, G. H. Brooke, Rational square-root approximations for parabolic equation algorithms, *The Journal of the Acoustical Society of America* 101 (2) (1997) 760–766. doi:10.1121/1.418038.
- [25] E. C. Titchmarsh, *The theory of functions*, 2nd Edition, Oxford University Press, London, England, 1976.
- [26] A. Royer, E. Béchet, C. Geuzaine, Gmsh-Fem: An efficient finite element library based on Gmsh, in: 14th WCCM-ECCOMAS Congress, 2021. doi:10.23967/wccm-eccomas.2020.161.
- [27] S. Balay, W. D. Gropp, L. C. McInnes, B. F. Smith, Efficient management of parallelism in object oriented numerical software libraries, in: E. Arge, A. M. Bruaset, H. P. Langtangen (Eds.), *Modern Software Tools in Scientific Computing*, Birkhäuser Press, 1997, pp. 163–202. doi:10.1007/978-1-4612-1986-6_8.
- [28] P. R. Amestoy, I. S. Duff, J. Koster, J.-Y. L’Excellent, A fully asynchronous multifrontal solver using distributed dynamic scheduling, *SIAM Journal on Matrix Analysis and Applications* 23 (1) (2001) 15–41. doi:10.1137/S0895479899358194.
- [29] D. M. Haider, H. De Gersem, J. Golm, T. Koettig, F. Kurian, N. Marsic, W. F. O. Müller, M. Schmelz, M. Schwickert, T. Sieber, R. Stolz, T. Stöhlker, V. Tympel, F. Ucar, V. Zakosarenko, Versatile beamline cryostat for the cryogenic current comparator (CCC) for FAIR, in: *Proceedings of the 8th International Beam Instrumentation Conference (IBIC’19)*, no. 8 in *International Beam Instrumentation Conference*, JACoW Publishing, Geneva, Switzerland, 2019, pp. 78–81. doi:10.18429/JACoW-IBIC2019-MOPP007.
- [30] P. Seidel, V. Tympel, R. Neubert, J. Golm, M. Schmelz, R. Stolz, V. Zakosarenko, T. Sieber, M. Schwickert, F. Kurian, F. Schmidl, T. Stöhlker, Cryogenic current comparators for larger beamlines, *IEEE Transactions on Applied Superconductivity* 28 (4) (2018) 1–5. doi:10.1109/tasc.2018.2815647.
- [31] Y. Boubendir, D. Midura, Non-overlapping domain decomposition algorithm based on modified transmission conditions for the Helmholtz equation, *Computers & Mathematics with Applications* 75 (6) (2018) 1900–1911. doi:10.1016/j.camwa.2017.07.027.